Universidade de Aveiro Departamento de Engenharia Mecânica
2014

Tiago André Cirne Ramos

Simulação numérica do processo de hidroformagem de componentes tubulares em múltiplas etapas

Numerical simulation of multi-stage hydroforming process of tubular parts

Universidade de Aveiro Departamento de Engenharia Mecânica
2014

Tiago André Cirne Ramos

Simulação numérica do processo de hidroformagem de componentes tubulares em múltiplas etapas

Numerical simulation of multi-stage hydroforming process of tubular parts

Dissertação apresentada à Universidade de Aveiro para cumprimento dos requisitos necessários à obtenção do grau de Mestre em Engenharia Mecânica, realizada sob orientação científica do Professor Doutor Robertt Angelo Fontes Valente, Professor Auxiliar do Departamento de Engenharia Mecânica da Universidade de Aveiro.

O júri / The jury

Presidente / President	**Doutor António Manuel de Bastos Pereira** Professor Auxiliar, Universidade de Aveiro
Vogais / Committee	**Doutor Hélder Tiago Carriço Mata (arguente)** Investigador de Pós-Doutoramento, Faculdade de Engenharia da Universidade do Porto
	Doutor Robertt Angelo Fontes Valente (orientador) Professor Auxiliar, Universidade de Aveiro

Agradecimentos / Acknowledgements

Ao Professor Doutor Robertt Valente, pela orientação, disponibilidade e motivação demonstrada durante todo o desenvolvimento desta dissertação.

Ao GRIDS pelas iniciativas organizadas que contribuiram directa ou indirectamente na elaboração deste trabalho, e em particular ao João Caseiro, pelo apoio dado nas simulações numéricas iniciais.

Aos meus amigos, com os quais caminhei nestes últimos anos de aprendizagem.

À minha família, em especial aos meus pais e irmãos pelo apoio incondicional, não só na conclusão desta etapa, mas em todo o meu percurso de vida. Muito obrigado!

Palavras-chave

Hidroformagem tubular; Cordão de soldadura; Simulação numérica, Método dos elementos finitos.

Resumo

Os processos de hidroformagem tubular caracterizam-se pela conformação plástica de estruturas metálicas tubulares através da conjugação de deslocamentos axiais de punções compressão e pressão interna. A correcta conjugação destes dois parâmetros permite que peças complexas, de espessuras variáveis, sejam obtidas. Adicionalmente, permite a obtenção de um excelente acabamento superficial, onde as propriedades mecânicas podem ser variáveis e ajustáveis consoante a aplicação em causa. Em termos de aplicabilidade a nível industrial, a hidroformagem tubular desempenha um papel crucial na indústria automóvel e aeroespacial, como sendo um processo atractivo no desenvolvimento de componentes estruturais mais leves sem perda de resistência estrutural quando comparado com processos convencionais. Nesta ótica, o recurso à simulação numérica para melhor compreensão e previsão de instabilidades inerentes ao processo (estricção e enrugamento) revela-se de máxima importância. No âmbito do presente trabalho, dois casos de estudo são abordados: (i) uma estrutura axissimétrica de secção circular variável, e (ii) um tubo em forma de T. Na definição dos modelos num ambiente de análise numérica por elementos finitos, recorrendo ao software Abaqus, curvas de carregamento de múltiplas etapas, assim como análises de sensibiblidades, no que toca a refinamento e tipo de malhas aplicadas, são conduzidas para averiguar os efeitos nas instabilidades referidas. Em ambos os casos de estudo são avaliadas a influência da consideração de um cordão de soldadura longitudinal, ao definir as propriedades mecânicas do material na zona do cordão e na zona afectada pelo calor. A presença de um cordão de soldadura é desprezada na maior parte das simulações da literatura por efeito de simplificação numérica, o que pode levar a aproximações mais grosseiras comparativamente com os resultados obtidos experimentalmente.

Keywords Tubular hydroforming; Weld seam; Numerical simulation, Finite element method.

Abstract Tubular hydroforming process is characterized by the plastic forming of metallic tubular components through the conjugation of compressive axial feeding and internal pressure. A proper definition of these parameters, known as loading path, allows the plastic forming of more complex parts, with variable thicknesses distributions. Additionally, the final part has excellent surface finishing and mechanical properties that may be adjusted towards the specified application. In terms of industrial products, tubular hydroforming plays a crucial role in automobile and aerospace industries, as an attractive process for production of lightweight structures, where structural stiffness is not compromised when compared to conventional forming processes. For that purpose, the use of numerical simulation based on finite element analyses, with the comprehension and prediction of the instabilities associated to the process (necking and wrinkling), is of maximum relevance. In this work, two benchmarks are taken into account: (i) a bulge tube with axisymmetric geometry, and (ii) a T-shaped tube. By defining the models in a numerical analysis environment by finite elements, using Abaqus software, loading paths with multiple stages, as well sensitivity analyses towards the type and mesh refinements applied, are conducted in order to evaluate the effects of the instabilities previously mentioned. In both benchmarks, it's also evaluated the influence of a longitudinal weld line by defining the weld bead and heat affected zone (HAZ) by means of their mechanical properties. The presence of this type of weld line is neglected in most of the research works in literature as a measure of simplification, which may lead to misleading results regarding the case when compared to those experimentally obtained.

Contents

List of Tables

List of Figures

Chapter 1

Introduction

Summary This chapter provides an introduction to the current Dissertation by outlining its main goals, as well as a guideline for the topics developed in each chapter of this document.

Tubular hydroforming process is defined as a plastic forming of metallic tubular structures through axial feeding and internal pressure synchronization. The correct definition and conjugation of these main parameters makes possible the forming of complex parts, with straight sections and variable thicknesses. Additionally, it allows an excellent superficial finishing with mechanical properties being adjustable according of the desired application. Several applications can be founded for tubular hydroforming, mainly in automobile and aerospace industries. More advanced features can be studied such as the hydroforming of dissimilar components composed of distinct materials and thicknesses obtained by welding, as well as the concept of the plastic forming in multiple stages. By this means, numerical simulation assumes a crucial role to predict and prevent typical failures associated to the process, such as wrinkling and necking problems, as well as springback effects in a shorter and more economical way relatively to studies supported only by experimental research.

1.1 Goals

The work developed in this dissertation intends to extend the knowledge of numerical simulation in technological processes, with particular focus on tubular hydroforming (THF) processes of metallic components. The main goals are summarized as the following:

- To study the available benchmarks in THF - bulge-shape and T-shape models - by identifying and evaluating defects such as buckling, wrinkling, necking (and bursting) and their relation with the process parameters;
- To study the influence of weld properties - weld bead and heated affected zone (HAZ) - in the previously mentioned instabilities by considering longitudinal welded tubular geometries in the numerical simulations;

- To conduct numerical sensitivity analyses of the developed models based on mesh refinements of tubes and dies;
- To understand the mathematical and computational concepts involved in modelling the elastoplastic behaviour of metallic components;
- To master the computational tools based on the Finite Element Method (FEM) and the corresponding software package chosen for this works, that is, Abaqus.

1.2 Guidelines

Besides the current chapter, where an introduction and description of the main goals are made, this dissertation comprise five more chapters, plus the Chapter 7 which is related to the final considerations.

Chapter 2, 3 and 4 are related to a summary of the state-of-art of tubular hydroforming, plasticity theory and numerical simulation by FEM, respectively. In Chapter 2, a highlight of the tubular hydroforming process is presented. Aspects such as applications, advantages and limitations, factors that influence the process and general failures modes are approached. A brief explanation of the role of tailor welded techniques is also given.

Chapter 3 introduces the basics concepts of the plasticity theory for phenomenological models, which comprises the concise description of yield criteria, isotropic and kinematic hardening laws and flow rules associated to metallic materials.

A summary of the Finite Element Method role in numerical simulations is taken into account in Chapter 4. It is mentioned a description of its general principles, as well as the presentation and explanation of three-dimensional elements properties (solid and shells) to apply in three-dimensional simulations, as well as the non-linearities inherent to plastic forming processes. In a second part of the chapter, it is described the Finite Element Analysis role on the developments of tubular hydroforming research. An overview of the software Abaqus is also carried out.

Chapter 5 and 6 represent the benchmarks carried out in this dissertation. Chapter 5 is relative to the axissymetric model benchmark and chapter 6 to the T-shaped model benchmark. In both chapters, a description of the benchmark and its conditions in the numerical environment are submitted. As mentioned before, sensitivity analysis are conducted in models with and without weld seam definition in order to analyse the effects in the instabilities relative to the hydroforming process in simulation environment. Consequently, the results of the numerical simulations are displayed and discussed in its corresponding chapter.

In Chapter 7 (Final Considerations) the conclusions of the developed work are presented and some future topics of research are proposed.

Chapter 2

Tubular Hydroforming

Summary This chapter approaches the industrial process of tubular hydroforming, being divided into several subsections, where an overview of the process is given. Additionally, a brief description of tailor welded techniques is given at the end of the chapter.

2.1 Historical background

Hydraulic forming or hydroforming, as it is mostly known, is a plastic forming process which relies on the imposition of a fluid pressure to shape the workpiece onto the corresponding die, instead of using the actual contact of a metallic punch as happens in conventional forming processes.

Hydroforming technology has made its first appearance at least in the pre World War II period, for sheet metal manufacturing. Tubular hydroforming (THF), on the other hand, appeared in the 70's being initially conceived for sanitary applications, although its theoretical background has been established back in the 1940's. Since the 90s, its presence in a large number of industries started to increase, especially in automotive industry, which has been promoting an extensive research work on the THF process and methodology. Currently, researchers use FEM simulations on THF as a standard development tool. Until nowadays, the process stands as an alternative method to conventional forming methods [1; 2; 3].

2.2 Description of the process

For an easy understanding of the process of tube hydroforming, an introduction of the machines general components is carried out in this sections. Based on Alaswad [4], the following scheme can be described:

1. *Presses or clamping devices:* they are used to open and close the die and to provide enough clamping load during the forming time to avoid elastic deflections and die separation. The dimension of the blank and the maximum internal pressure dictate the tonnage of the press, since it is dependent on the required closing force;

2. *Tooling:* they typically involve the die holders, dies and inserts. Tools made of high strength material, with quality on the surface finish, interchangeable inserts, good guiding systems and balanced design (to minimize the closing forces) are specifications of great importance for hydroforming equipments.

3. *Pressure system:* they are represented by a pump, an intensifier and control valves being designed to guarantee the imposed pressures levels in a wide range of parts.

4. *Axial hydraulic cylinders and plungers:* the axial plungers provide the necessary feed force to push the material into the expansion regions and avoid any pressure loss from the die, sealing the ends of the tube.

The principle of THF process is easily comprehended by a few main steps, as shown in Figure 2.1. The scheme represents a T-shaped piece production and it is described in the following. Firstly, a hydraulic press is equipped with dies and the tube is inserted into one of the dies. In order to seal the extremities of the tube, the axial sealing punches are aligned, followed by the closing of the dies. The filling of the tube's cavity is initiated with a fluid medium through one of the sealing punches. The used fluid medium is typically a mixture of water and an oil or synthesis-based emulsion additive, which provides corrosion inhibitors, anti-foam/bacterial agents and a lubrication source in certain cases [5]. The combination of axial displacement of the punches and the internal pressure enables the forming of the desired component shape. For this particular example, a counter-punch is applied to control the material flow. A pressure calibration stage is often performed to guarantee the contour of the final piece. The die is finally opened and the formed component is removed.

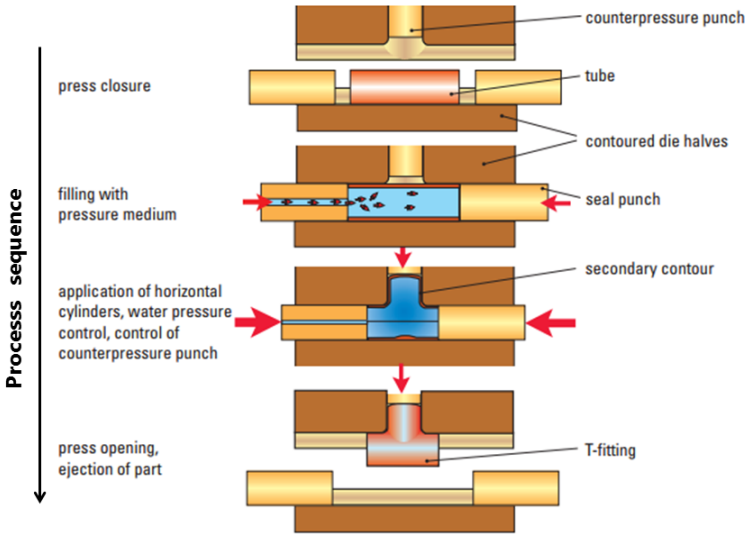

Figure 2.1: Tubular hydroforming process sequence [6]

2.3 Applications

Tube hydroforming already presents itself as a well established technology, due to the very complex shapes that can be obtained at sustainable costs when comparing with conventional technologies. This technology can be mainly found in automotive and the aerospace industries, as well as in the manufacturing of household components for sanitary use, for example. In the automotive field, the first applications have been non-structural components from exhaust and intakes systems: cooling pipes, tail pipes, pressure tubes, connectors and manifolds. Normally, those parts are made of stainless steel in order to be in accordance to structural, thermal and corrosion properties [7; 8].

Along the last years, applications in structural components, such as the Body-in-White (BIW) in the automobile industry has transformed into a reality. BIW is the name given to the stage where the car's metallic body components have been welded together, but not including any moving part such as doors fenders, etc. Examples of hydroformed parts associated with body and safety are A/B/C pillars, windscreen headers, space frame components, seat frames and shock absorbers housings [9]. Other components belonging to the chassis category, such as the roof and lower rails, side frames, instrument panels, rear axle frames and radiator frames were also explored between different vehicles and brands [8]. For instance, the engine cradles (sub-frames) proved to be a turning point for the application of tube hydroforming in large volume production in the automotive industry. In Figure 2.2, exhaust and rear axle components are shown as integrated in BMW M3, being obtained by tube hydroforming. Ford is driving increased use of hydroformed components across its global structures. In 2003, Ford process-designers were able to downsize the production of the front end of the F-250 pickup model by eliminating 18 stamping operations for 9 other operations, including hydroforming ones. Not only they experienced a significant reduction in spot welds, but also in the component mass, the diference between the first design to the third generation being from 42 kg to 26 kg. More recently, Ford engineers claim to be the world's first to achieve hydroformed steel tubes for its B-pillars, displayed in Figure 2.3. The side-impact performance was greatly improved and the tubes showed lower deformation levels and a better overall control over it [10].

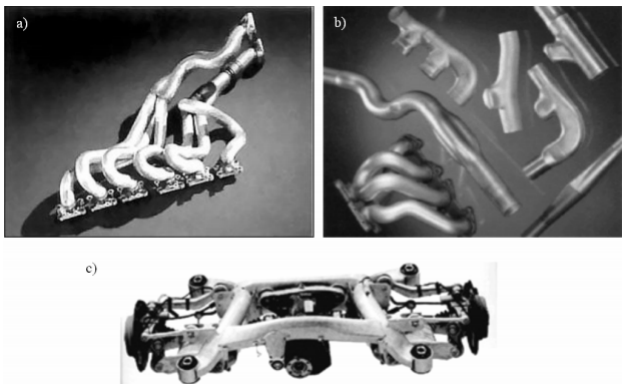

Figure 2.2: BMW M3 (a) exhaust system (b) and its elements formed by hydrofoming (c) as well as the rear axles with hydroformed components [9].

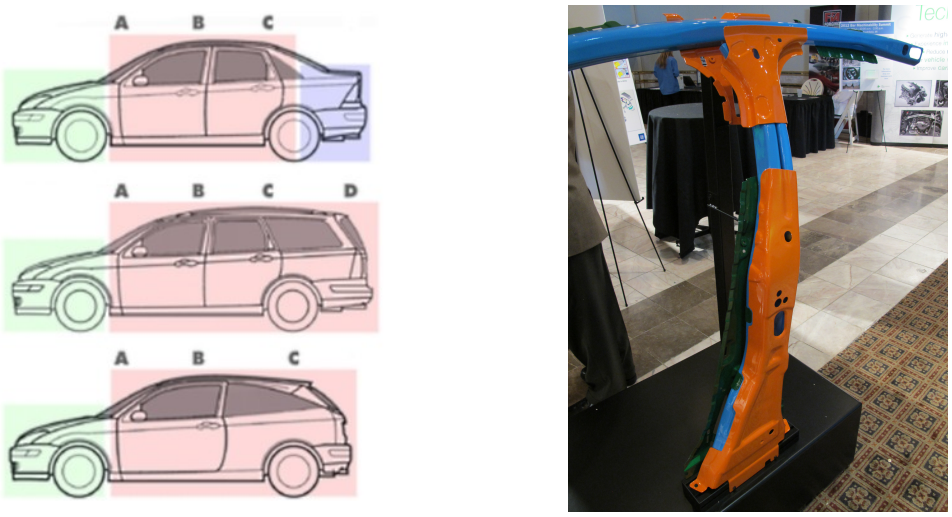

(a) (b)

Figure 2.3: Pillars: a) position scheme [11]; b) Ford Fusion hydroformed B pillar - Blue vertical part [10]

2.4 Advantages and drawbacks

Several advantages from the point of view of the part and process performance can be achieved by tube hydroforming when compared with conventional manufacturing through stamping [12].

Among the most important ones, the formed workpiece can have a higher quality, which leads to tighter tolerances, enhanced surface finishing, weight reduction (via more efficient design) and improved structural strength and stiffness. Additionally, THF allows for a better part consolidation, as the parts to be formed may be more than one welded hollow piece.

The manufacturing costs can be also reduced due to a lower number of forming and assembly operations, lower tooling costs due to less tools required, fewer secondary operations and less waste. Operations such as piercing a hole can be attained while the hydroforming process is occurring.

Nevertheless, this technology has some disadvantages which may limit their application for some cases. In order to make the best use of THF, one must be aware of its drawbacks and limitations.

THF may require less steps to form a part but demands more time on the execution which is crucial in mass production lines. The implementation of operations such as bending and piercing can contribute to downsize the forming period, however in presents slower cycle time in operations comparatively to conventional forming processes. On the other hand, equipments such as hydraulic presses represents an high investment, which one must has into account when considering use this type of metal forming process. Finally, other disadvantage of hydroforming, which has been reduced during the last decade, is related to the lack of extensive knowledge of the process available to product and process designers.

2.5 Factors affecting the process

To achieve the production of successful formed components with the required quality, there are some factors that must be taken into account. Material properties, friction, lubrication and project conditions or specification of the pre-forming, axial feeding and internal pressure are some of them.

2.5.1 Material properties

From the overall parameters involved in THF, a detailed knowledge of the material properties play a dominant role in the success of the hydroforming product obtained.

The same materials properties that are relevant for conventional stamping and extrusion process, such as anisotropy coefficients, yield stress, elongation and other strength indicators, are also valid for hydroforming operations success. More specifically, the ideal material should possess: low anisotropy, good superficial finishing (free of scratches), high and uniform elongation, high exponential hardening and low mechanical properties dispersion between the base material and the heat affected zone (HAZ) for the welded tubes [8].

All the alloys applied in extrusion or deep drawing such as stainless steels, alloyed steels and aluminium alloys are suitable for the process.

2.5.2 Friction and lubrication

Friction and lubrication conditions are also crucial for the performance of the hydroforming process, specifically at the final stage where there is no more movement of the tube extremities and the final adjustments of the material are done merely by the internal pressure. Nevertheless, these conditions are also beneficial during other stages of the process, allowing the material to more easily flow into the die cavity. For instance, good hydroforming lubricant conditions should be selected based on the following criteria, according to Muammer and Taylan [8]:

- lubricity, to reduce sliding friction between tooling and tube surface;
- durability under high pressure at tube-to-tooling interface, to prevent sticking and galling;
- minimum abrasivity, to reduce tool wear;
- compatibility with pressurizing medium and environmental requirements;
- ease of application and removal (washable);
- costs.

2.5.3 Project conditions

In some cases, tubes require pre-forming operations to approximate the contours shape to the final result, depending on their complexity. Throughout the preforming operation, no wrinkles or localized buckles are admitted in bending regions for hydroforming applications. Also, prevention of surface marks and significantly wall thinning and ovality is essential.

Another project condition is the number of stages executed. Since not all the parts can be obtained through a single stage of internal pressure and axial feeding, an optimal combination of these parameters in different stages is needed to accomplish an ideal formed part free of defects.

2.6 General failures

The appearance of failures in THF process can result of an inaccurate balance between the main parameters, that are internal pressure and axial feeding (Figure 2.4 a)). These failures can be divided in the following classes:

- *Buckling* - the danger of buckling prevails at the start of the operation by using an excessively high axial compressive force acting on the tube and it is mostly verified in long tubes with thick walls. Nevertheless, the risk of buckling must be countered during the entire start-up phase [1].

- *Wrinkling* - the formation of wrinkles is common in THF processes (Figure 2.4 b) in the top). Wrinkles are formed due the quick displacement of the axial cylinders or low internal pressure values comparatively to the associated axial feeding, causing excessive thickening. According to Lang [13], those are nevertheless "harmful" wrinkles. The "useful" ones can ease the formability, allowing its optimization in the different stages and being easily eliminated with additional pressure.

- *Bursting* - it happens when the tube walls are not able to withstand the internal pressure and, consequently, burst (Figure 2.4 b) in the bottom). As already mentioned, it starts with localized necking/thinning. This type of failure will not happen once the tube wall is resting against the tool, when the critical pressure state is reached [1].

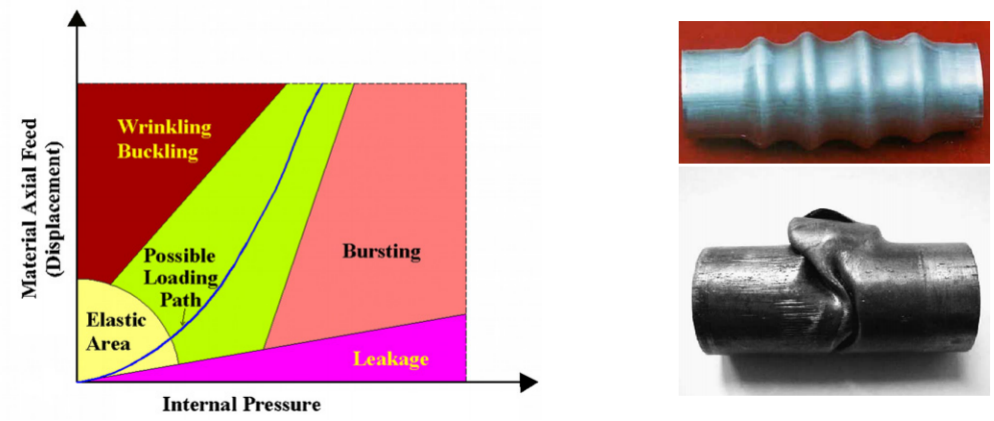

(a) (b)

Figure 2.4: Instabilities identification: (a) appearance according the loading path defined [14] (b) examples of a wrinkled tube (top) and a burst tube (bottom) [15].

2.7 Classification of THF components and process

Following Ghosh *et al.* [14], a review based on commercially available THF components was accomplished considering that they regard both axial feed and internal pressure. Following this, as it is demonstrated in Figure 2.5, the seven families can be designated in this form: bulge shape(B), Single Y Shape (SY), Aligned Double Y Shape (DY), Single T shape (ST), Aligned Double T shape (DT), Non Aligned Double T shape - opposite side (DTOS) and Non Aligned Double T shape - same side (DTSS).

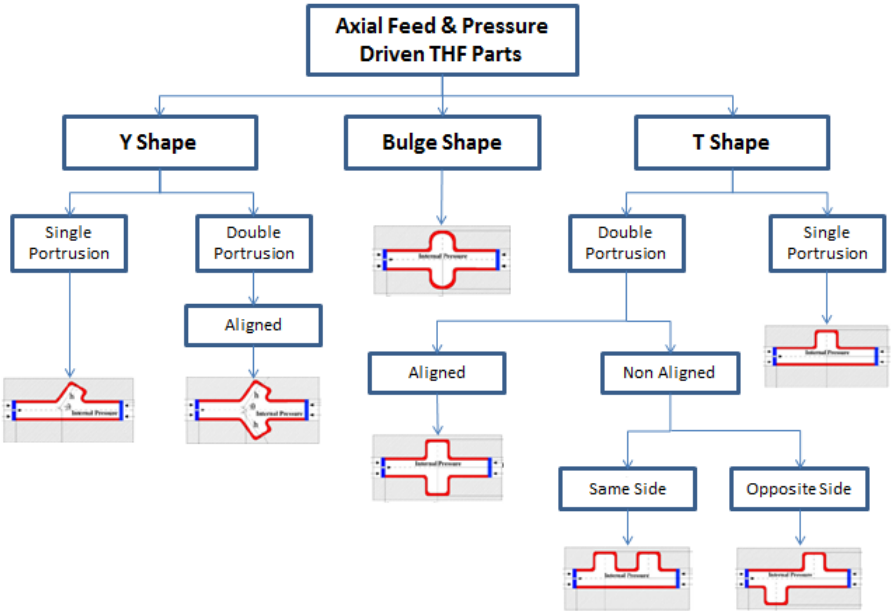

Figure 2.5: Classification of axial feed and pressure THF components, adapted from [14].

Related to the process, a simple classification relying on the importance of the main parameters associated (internal pressure and axial feeding) may be defined, as described by Ponce [16]:

- *Tube hydroforming by pressure only*: this type of process only requires the pressure to execute the forming of the component, typically one where the thinning effect is low, which implies that the risk of wrinkling or buckling are minimum. Nevertheless, due to the great force caused by the internal pressure on the axial plungers, the risk of leakage is increased. The main failure mode during the process operation is bursting;
- *Pressure-dominated tube hydroforming* : compared with the previous THF mode, it possesses a significant increase in the tube's expansion, which leads to the need of an axial flow of the material in order to achieve a successful ending part. As previously described, axial displacement is used to promote the creation of "useful" wrinkles, which can be removed with additional pressure. However, associated with a drastic expansion, the sensitivity to necking and bursting will arise even without an increase of internal pressure. Plus, an uncontrolled expansion might also lead to a retraction at the tube extremities resulting in the fluid's leakage;

- *Displacement-dominated tube hydroforming*: the displacement through axial punches is significant whereas the component would be impossible to be formed solely by the internal pressure of a fluid. Structural components with T, Y and X shapes are the typical examples for this group. The operational range of internal pressure is wide;

- *Tube hydroforming by axial feeding only*: the main purpose of the pumping system in this process is to fill and pressurize the fluid into the tube's cavity. The necessary pressure for forming will come by the axial feeding. To achieve a safe displacement choice, a pressure relief valve attached to the pressure supply line is used to remove some of the fluid in order to control the expansion volume.

2.8 Tailor welded techniques

There are a few methods to manufacture tube for hydroforming applications. For instance, tubes may be obtain through extrusion process, which enables a uniform material properties but poor thickness consistency. Nevertheless, tubes can also be formed from metal sheets using rolling and joining methods, featuring much more thickness consistency. Due to the welding process, the base material properties along the weld seam are no longer preserved, i.e. the material is strengthened at the weld seam, showing different properties from the parent material. According to Ripodas [17], the most common forming and welding processes of tubes to hydroforming applicaitons are:

- *Continuous roll-forming:* a metal strip is continuously rolled into a tube shape, whose longitudinal gap is simultaneously welded by high-frequency (HF) process. The weld seam is produced by inductive heating and compression of the edges of the metal strip. Alternatively, laser welding process can be also applied, leaving a reduced heat-affected welded zone ;

- *Cold-drawing:* the tubes obtained from continuous roll-forming or extrusion process are reduce into a new tube with a new diameter and thickness, by means of an internal and external mandrel;

- *Discontinuous forming:* a metal sheet is folded piece by piece, and welded by laser. The blanks used may be tailored.

Regarding the blanks specifications, the development of Tailor welded blanks (TWB) presents to be an attractive technique for sheet or tube hydroforming applications, in alternative to conventional manufacturing processes. The TWB's are semi-finished parts that consists in ,at least, two metals sheets of possible different thickness, material and surface coatings, as it is shown in Figure 2.6. This technique was developed to reconvert the use of the sheets leftovers.

Consequently, the ability of associate dissimilar components to others enhances the advantages in optimization component performance. Local stiffness is increased and weight reduction is achieved, features that are extremely attractive in aerospace and automotive industries. Also, the joining methods used before in forming the components results in production costs. The weld seam can be linear or non-linear, and non-linear weld seams are also called Engineered Blanks. Recently, strict regulations in pollution

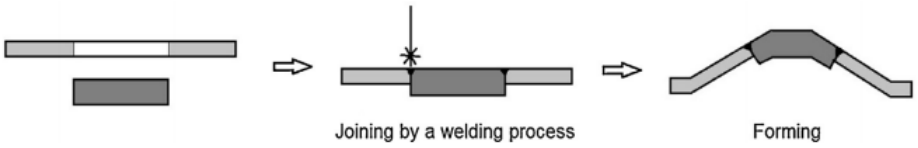

Figure 2.6: Principle of tailor welded blanks [18].

control and environment safety laws contribute for a major attraction of automobile industry over hydroforming and TWB technology [18; 19].

Tailor Welded Tubes (TWT) is the tubular version of the TWB. In other words, the initial tube blank is obtained from two or more tube segments with different thickness, material and coatings, providing structural advantages in tubular hydroformed applications. Some examples of TWT obtained by laser welding are displayed in Figure 2.7. Beside roll-forming and longitudinal welding as already mentioned, tubes may be directly welded by butt welding techniques or even welded with a sleeve, where this sleeve can be aligned with the outer or inner diameter, or still be added to reinforce the tube in a specific location [20].

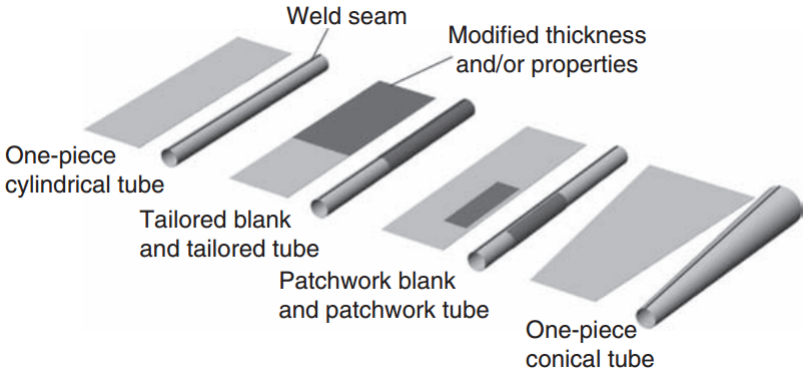

Figure 2.7: Examples of laser-welded tailored semifinished products [5].

Chapter 3

Plasticity theory

Summary In order to describe the material in a numerical simulation of forming process, one must be familiar to plasticity theory behind the constitutive models. In this chapter, basic concepts such as yield criteria, hardening laws and flow rules mathematical formulations are addressed.

3.1 Introduction

In a variety of forming technological processes, the behaviour of the material is identified as elastoplastic. In other words, as a material is loaded beyond its elastic limit, Hooke's law does not apply, the material yields and begins to flow with residual deformation appearing after unloading. This last behaviour is known as plasticity. By means of an uniaxial tensile test, the identification of the yield limit (σ_Y) is feasible due to the linear behaviour shown at the beginning of the loading path. Still, the overall of the technological processes is subjected to multiaxial stress states which implies a more complex definition of the yield limit.

Plasticity mechanisms are the result of atomic defects - dislocations, and it may be characterized by two types of models: based on crystal plasticity models (microscopic domain) and phenomenological models (macroscopic domain). The latter offer a simpler and satisfactory approach of the problem in many applications. Therefore, the phenomenological or continuum models are in focus in this chapter and crystal models are not addressed.

3.2 Elemental concepts

Considering an elatoplastic model, the total strain,$\boldsymbol{\varepsilon}^t$, can be decoupled into two parts according to

$$\boldsymbol{\varepsilon}^t = \boldsymbol{\varepsilon}^e + \boldsymbol{\varepsilon}^p, \tag{3.1}$$

where $\boldsymbol{\varepsilon}^e$ are the elastic strain and $\boldsymbol{\varepsilon}^p$ are the plastic strain. This assumption is only valid for small deformations and not for large ones. Despite large variation in the initial

shape of the component to form in process such as hydroforming, this additive is applied in simulations of forming processes. Also due to the iterative and incremental approach, great levels of deformations are not obtained during the successive stages of forming.

In the elastic domain, the Hooke's law states that the stress tensor, $\boldsymbol{\sigma}$, may be linearly related to the elastic strain, in the form

$$\boldsymbol{\sigma} = \mathbf{D} : \boldsymbol{\varepsilon}^e, \tag{3.2}$$

where $\mathbf{D}$ represents the 6x6 elasticity tensor for isotropic materials

$$\mathbf{D} = \frac{E}{(1+\nu)(1-2\nu)} \begin{bmatrix} (1-\nu) & \nu & \nu & 0 & 0 & 0 \\ \nu & (1-\nu) & \nu & 0 & 0 & 0 \\ \nu & \nu & (1-\nu) & 0 & 0 & 0 \\ 0 & 0 & 0 & \frac{(1-2\nu)}{2} & 0 & 0 \\ 0 & 0 & 0 & 0 & \frac{(1-2\nu)}{2} & 0 \\ 0 & 0 & 0 & 0 & 0 & \frac{(1-2\nu)}{2} \end{bmatrix}, \tag{3.3}$$

where E is the Young modulus and ν is the Poisson's coefficient.

To describe the plastic deformation according phenomenological models, the follow aspects must be considered [21]:

1. A yield criterion, to evaluate the beginning of plastic deformation zone based on the stress tensor;

2. A hardening rule, to describe the evolution of the yield limit according to the degree of plastic strains;

3. A flow rule to define the relation between the stress field and plastic strains.

These aspects are separately addressed in the next sections.

3.3 Yield criteria

The definition of the yield surface according to the phenomenological models is supported by a yield criterion. In general, such criterion may be formulated by means of a plastic potential, expressed by

$$F(\boldsymbol{\sigma}, \boldsymbol{\alpha}) = 0, \tag{3.4}$$

which is a function of the stress tensor ($\boldsymbol{\sigma}$) and a vector $\boldsymbol{\alpha}$, whose variables are obtained experimentally, influencing the hardening.

For isotropic materials with isotropic hardening, where the yield surface solely depends of the principal stresses, it is possible to separate the stress contributions and the hardening variables in independent terms,

$$F(\boldsymbol{\sigma}, \boldsymbol{\alpha}) = f(\boldsymbol{\sigma}) - \sigma_Y(\boldsymbol{\alpha}) = 0, \tag{3.5}$$

where $f(\boldsymbol{\sigma})$ is a mathematical convex function of the stress tensor (known as the yield function), while $\sigma_Y(\boldsymbol{\alpha})$ is the hardening term that establishes the yield surface dimension.

The physical interpretation of $f(\boldsymbol{\sigma})$, also designated by effective stress ($\bar{\sigma}$) can be seen by means of an uniaxial tensile test.

Taking into account the equation 3.5, any yield criteria is independent of the referential position. By this means, it can be expressed in terms of three stress invariants:

$$f(\boldsymbol{\sigma}) = f(I_1, I_2, I_3), \tag{3.6}$$

where

$$\begin{aligned} I_1 &= \mathrm{tr}(\boldsymbol{\sigma}) = \sigma_{ii}, \\ I_2 &= \frac{1}{2}\mathrm{tr}(\boldsymbol{\sigma}^2) = \frac{1}{2}\sigma_{ij}\sigma_{ji}, \\ I_3 &= \frac{1}{3}\mathrm{tr}(\boldsymbol{\sigma}^3) = \frac{1}{3}\sigma_{ij}\sigma_{jk}\sigma_{ki}. \end{aligned} \tag{3.7}$$

Since the hydrostatic tensor is assumed not to affect the yield function [22], an isotropic criterion may be defined by the second and third invariant of the deviatoric tensor, $\mathbf{S}$, by

$$\mathbf{S} = f(J_2, J_3) = \sigma_{ij} - \frac{1}{3}\sigma_{ii}\delta_{ij}, \tag{3.8}$$

where the invariants of the deviatoric tensor are

$$\begin{aligned} J_2 &= \frac{1}{2}\mathrm{tr}(\mathbf{s}^2) = \frac{1}{2}s_{ij}s_{ji}, \\ J_3 &= \frac{1}{3}\mathrm{tr}(\mathbf{s}^3) = \frac{1}{3}s_{ij}s_{jk}s_{ki}. \end{aligned} \tag{3.9}$$

For a given point of the material body, the following interpretations for the scalar $F(\boldsymbol{\sigma}, \boldsymbol{\alpha})$ are assumed:

- If $F(\boldsymbol{\sigma}, \boldsymbol{\alpha}) < 0$, the material shows an elastic behaviour;
- If $F(\boldsymbol{\sigma}, \boldsymbol{\alpha}) = 0$, the material shows an plastic behaviour;
- If $F(\boldsymbol{\sigma}, \boldsymbol{\alpha}) > 0$, this condition has no valid meaning (although numerically possible to be obtained).

Graphically, the previous statements can be expressed in the three-dimensional Haigh-Westergaard stress space. This space is represented by three mutually orthogonal axis, whose coordinates are the principal stress values [23]. Figure 3.1 displays the yield limit surface resulting of the application, as examples of Tresca and von Mises yield criteria.

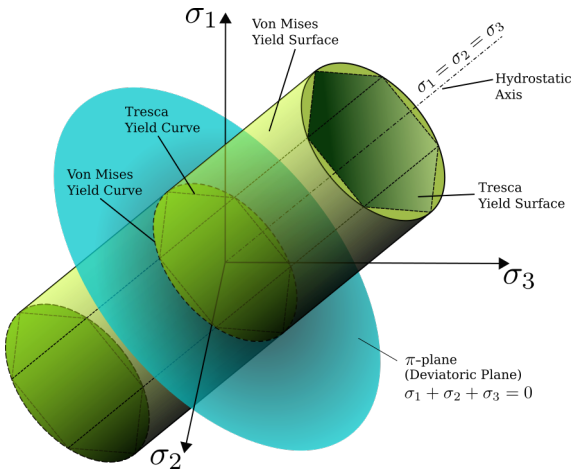

Figure 3.1: Geometric representation of Tresca and von Mises yield criteria in Haigh-Westergaard stress space [24].

3.3.1 Tresca criterion

The formulation of Tresca (1864) enunciates that plastic deformations occurs when a maximum shear stress, τ_{max}, surpass a critic value [22],

$$\tau_{max} = \frac{\sigma_1 - \sigma_3}{2} = k^* \quad \text{and} \quad \sigma_1 - \sigma_3 = \sigma_Y, \tag{3.10}$$

where σ_1 and σ_3 are the principal stress tensors, with $\sigma 1 \geq \sigma 2 \geq \sigma 3$, and k^* is a specific material parameter which is determined experimentally through uniaxial tests (tensile or compression) and can be function of the hardening.

3.3.2 Von Mises criterion

The formulation of von Mises yield criterion (1913) considers that the plastic deformation occurs when the distortion part of the elastic energy per volume of unit reaches a critic value [22]. In mathematical form, this value is related with the second invariant of the deviatoric stress tensor, as

$$\sigma_Y = \sqrt{3J_2}. \tag{3.11}$$

The limit value is determined by assuming an uniaxial tensile state, $\sigma_1 = \sigma_Y$, $\sigma_2 = \sigma_3 = 0$. In the Haigh-Westergaard space, the radius of the cylinder surface for von Mises is $\sqrt{\frac{2}{3}}\sigma_Y$.

3.4 Hardening laws

In a summary form, it will be presented the laws that influence the yield surface evolution according the plastic deformation, being called hardening laws. By this means, a random material point is considered for which it is known the initial yield surface and this will be reshaped along the plastic deformation: expand or contract, move or distort in a non-uniform way. If the yield surface stands unchanged, i.e no existence of hardening,

the material has an elasto-perfectly plastic behaviour (Figure 3.2 a). Figure 3.2 b), on the other hand, corresponds to a material that exhibits hardening behaviour.

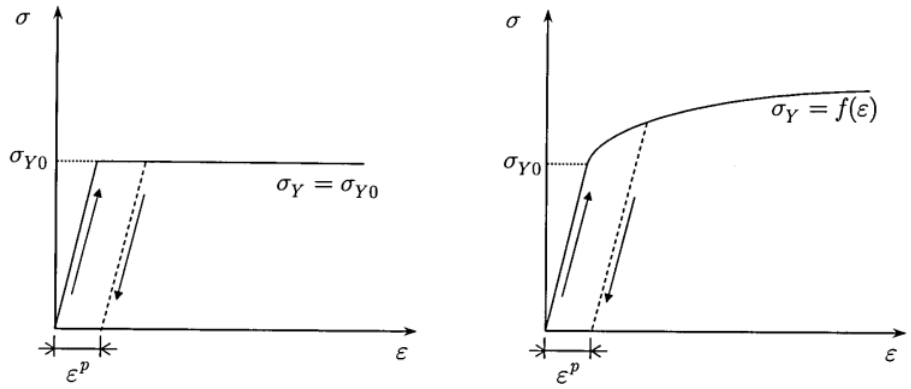

(a) (b)

Figure 3.2: Elastoplastic behaviour of a typical tensile test: a) with no hardening; b) with hardening [25].

These macroscopic laws are under dependency of certain internal variables of material like the effective plastic strain, $\bar{\varepsilon}^p$, and the plastic work, W^p, which are independent of the strain path. The effective plastic strain is given by

$$\bar{\varepsilon}^p = \int \mathrm{d}\bar{\varepsilon}^p, \quad \text{where} \quad \mathrm{d}\bar{\varepsilon}^p = \sqrt{\frac{2}{3}\varepsilon^p_{ij}\varepsilon^p_{ij}}, \tag{3.12}$$

with $i, j = 1, 2, 3$, while the plastic work is defined by

$$W^p = \int \sigma_{ij}\mathrm{d}\varepsilon^p_{ij}. \tag{3.13}$$

The main hardening modes are the isotropic hardening (isotropic expansion of the yield surface) and kinematic hardening (translation of yield surface). The combination of both modes is named as mixed hardening, which describes the material behaviour in a more general form.

3.4.1 Isotropic hardening

The generic yield surface with isotropic hardening solely depends of the effective plastic strain as can be seen in the following expression

$$\Phi(\boldsymbol{\sigma}, \bar{\varepsilon}^p) = \phi(\boldsymbol{\sigma}) - \sigma_Y(\bar{\varepsilon}^p) = 0. \tag{3.14}$$

The concept of isotropic hardening is easily understood by looking at the Figure 3.3. At the Figure 3.3 a), the material, under a tensile load, behaves elastically until point A. When the limit of elasticity is surpassed, the material presents an elastoplastic behaviour and the yield surface expands isotropically. In point B there is a switch of the load direction (compression load) and a new yield limit surface is introduced. Naturally, the material has a perfectly elastic behaviour from B to C and, by surpassing this last point,

the material will restart hardening again. At the Figure 3.3 b), the same path is described along the yield surface evolution.

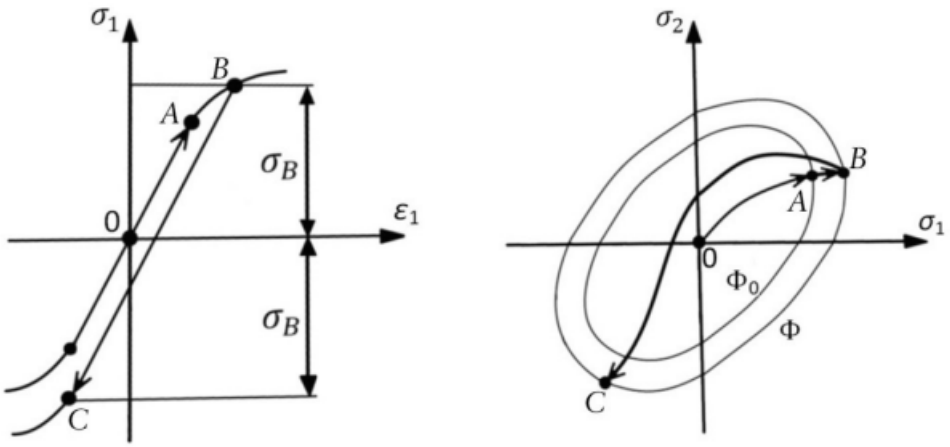

(a) (b)

Figure 3.3: Representation of isotropic hardening: a) uniaxial tensile load followed by compression; b) biaxial representation of a load followed by compression [26].

Several authors have proposed different equations to describe isotropic hardening behaviour. Among them, the most relevant are cited here [27]:

- Ludwick (1909), $\sigma_Y = \sigma_{Y_0} + H\bar{\varepsilon}^n$
- Prager (1938), $\sigma_Y = \sigma_{Y_0} \arctan \frac{E\bar{\varepsilon}}{Y_0}$
- Hollomon (1944) , $\sigma_Y = H\bar{\varepsilon}^n$
- Swift (1947), $\sigma_Y = C(\varepsilon_0 + \bar{\varepsilon}^p)^n$
- Voce (1948), $\sigma_Y = \sigma_{Y_0} + R$, where $\dot{R} = C_y(Y_{sat} - R)\dot{\bar{\varepsilon}}^p$ and $R(0) = 0$
- Fernandes *et al.* (1998), $Y = C[g(\varepsilon_0 + \bar{\varepsilon}_{ps}) + h\bar{\varepsilon}^{p*}]^n$

where σ_Y and σ_{Y_0} are the yield stress and the initial yield stress at an uniaxial tensile condition.

Particularly for the Swift and Voce models, the parameters C, n, R, C_y, Y_{sat}, are material constants which can only be measured experimentally. The Swift law equation can describe more properly the behaviour of materials whose isotropic hardening do not present signs of saturation, ie describes a pure isotropic hardening. Based on experimental results, it is suited to properly describe steels. On the other hand, the Voce law is more appropriated for materials that exhibit isotropic hardening with saturation, as in the case of aluminium alloys, for instance.

3.4.2 Kinematic hardening

The kinematic hardening law dictates the evolution of the position of the yield surface center as function of the plastic strain. Mathematically, this can be modelled by taking

into account a stress tensor $\mathbf{X}$, designated by "back stress". The generic yield surface with kinematic hardening, associated with the effective plastic strain, may be written as

$$\Phi(\boldsymbol{\sigma}, \bar{\varepsilon}^p) = \boldsymbol{\phi}(\boldsymbol{\sigma} - \mathbf{X}(\bar{\varepsilon}^p)) - \sigma_{Y_0} = 0 \tag{3.15}$$

The kinematic hardening concept can be illustrated in Figure 3.4 a) and b). It follows an identical behaviour as the isotropic example (Figure 3.3) when subjected to an uniaxial tensile force (point B). Once the direction is inverted, the yield surface limit is achieved as soon as the stress difference in elastic state equals the double of stress value at the initial elastic limit.

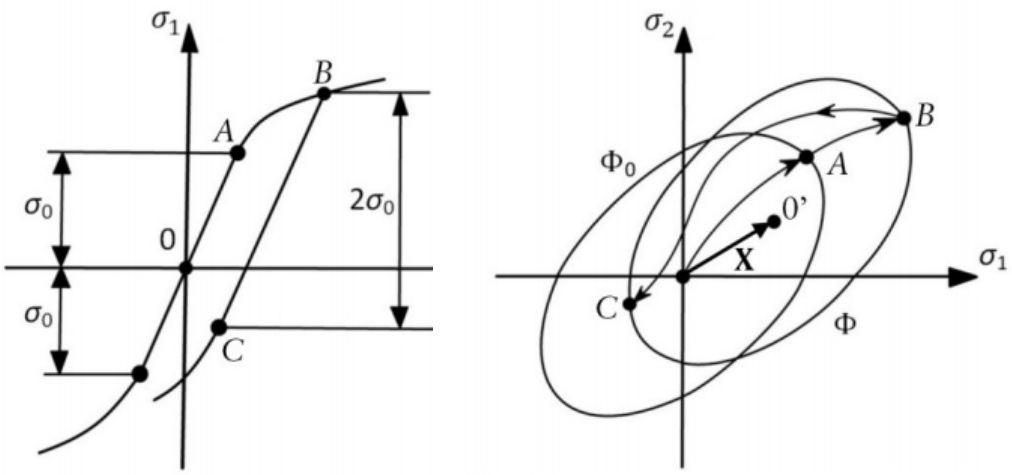

(a) (b)

Figure 3.4: Representation of kinematic hardening: a) uniaxial tensile load followed by compression; b) biaxial representation of a load followed by compression [26].

3.4.3 Mixed hardening

Finally, the combination of both laws enables a more generic description of the material's behaviour. As already mentioned, the law is known as distortional hardening or, more commonly, mixed hardening. The formulation of its yield surface is given by

$$\Phi(\boldsymbol{\sigma}, \boldsymbol{\alpha_1}, \boldsymbol{\alpha_2}) = \boldsymbol{\phi}(\boldsymbol{\sigma} - \mathbf{X}(\boldsymbol{\alpha_1})) - \sigma_Y(\boldsymbol{\alpha_2}) = 0, \tag{3.16}$$

where α_1 and α_2 are the kinematic and isotropic variables, respectively.

3.5 Flow rules

The yielding criterion and the hardening law describe the yield surface and its evolution as function of the plastic deformation, respectively. Nevertheless, both lacks in information on how the plastic strain evolution is conducted. The flow rule defines the increments and directions of the plastic strain according to the stress state and its increments. The

flow rule which more realistically defines the material's behaviour is the non-associative flow rule [28], in the form

$$\mathrm{d}\varepsilon_{ij}^{p} = \frac{\partial Q}{\partial \sigma_{ij}}\mathrm{d}\lambda, \tag{3.17}$$

where Q is the plastic potential, σ_{ij} is the stress tensor components and $\mathrm{d}\lambda$ is a scalar value named plastic multiplier, whose purpose is to adjust the size of plastic increments. Since the plastic deformation is irreversible, $\mathrm{d}\lambda$ necessary positive during plastic flow [29]. Once the hydrostatic stress influence the material's plastic behaviour, the plastic potential surface is distinct of the yield surface ($Q \not\equiv F$).

However, for the majority of metallic materials, the plastic flow is not significantly affected by the hydrostatic stress. Taking that into account, the plastic potential can be represented by the yield function ($Q \equiv F$) which corresponds to the associative flow rule,

$$\mathrm{d}\varepsilon_{ij}^{p} = \frac{\partial F}{\partial \sigma_{ij}}\mathrm{d}\lambda, \tag{3.18}$$

where $\partial F/\partial \sigma_{ij}$ is the plastic deformation rate tensor, also called yield vector. The associative flow rule considers that the plastic strain increments are orthogonal to the yield surface, which is also known as the normality condition. The flow rules mentioned can be schematically represented in the Figure 3.5 a).

As a summary, the three cases of strain hardening can be given as [23]:

- For $\mathrm{d}F < 0$ the material is elastically unloading. The yield vector aims towards the inner of the yield surface and reverse from plastic to an elastic state;
- For $\mathrm{d}F = 0$, the stress state is situated on the yield surface which dictates a perfectly plastic material's behaviour, know as neutral loading;
- For $\mathrm{d}F > 0$, this represents a loading situation and by surpassing the yield surface limit, the plastic strain develops non-linearly, a representative situation of a hardening behaviour.

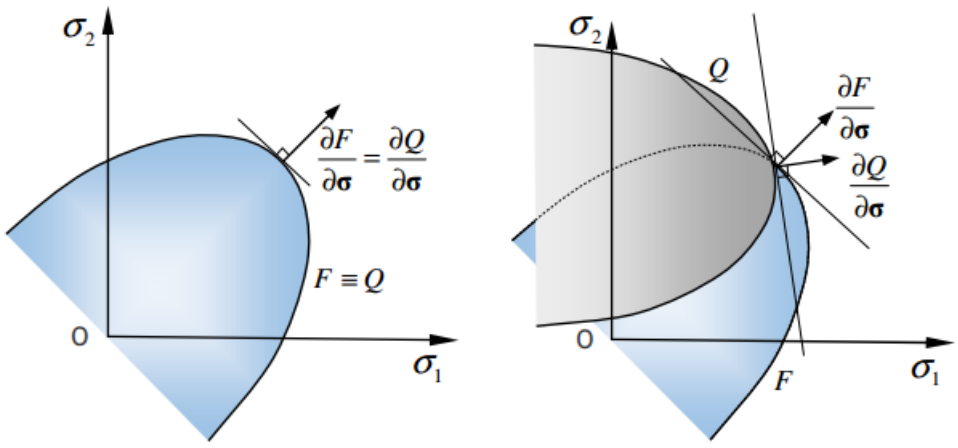

(a) (b)

Figure 3.5: Scheme of the flow forms: a) associated; b) non-associated [28].

Chapter 4

Numerical simulation by FEM

Summary Finite element numerical tools play an important role on the study of metal forming processes. By this means, an overview of the Finite Element Method (FEM) is carried out in the first part of this chapter. The second part is focused on the application of FEM in industry and research case studies, particularly in tubular hydroforming, by describing some of the works on this field.

4.1 Finite element method

4.1.1 Historical background

As often associated with original developments, define an exact "birth of the invention" can be difficult. However, the first paper (1943) incorporating the principles of the FEM as it is known nowadays belongs to Courant [30]. Courant, an applied mathematician, analysed torsional problems of a hollow shaft by dividing the cross sectional in triangles - method know as "discretization". Simultaneously, other research groups of other fields were also interested in FEM development such as physicists - J.L. Synge and engineers - J.H Argyris and S. Kelsey [31]. In 1956, the work developed by Turner and co-authors proved to be one of the key contributions for the advances in future FEM research [32]. The work presents the first finite element formulation ever defined: one generic quadrilateral, one triangular element and also a rectangular element. However, the term finite element was not yet use at the time. It was only coined for the first time in literature by Ray Clough in 1960 [33].

Over the following decades, an intensified element research on the FEM was conducted in Europe and United States. Also, the development and rapidly increasing use of some computer programs (such as ASKA, NASTRAN and SAP) clearly contributed for the advancement and acceptance of the method [34]. Taking into account these factors, new algorithms, finite element programs and theories started to be developed. Nowadays, the Finite Element Method is accepted as a widely and indispensable tool analysis in a vast range of industries and applications.

4.1.2 FEM concept

The Finite Element Method (FEM) is by far the most accepted technique for numerical simulation of sheet metal forming, proving to be a powerful mathematical method of analysis for scientific and engineering problems. This method enables the modelling of a generic continuum model by means of a discretization process: the subdivision of the main model into smaller discrete components, for which it is possible to get a mathematical description.

Thus, FEM's users when confronted with a complex problem, where it is impossible or extremely arduous to apply an analytical global approach, may solve it by adopting a structured and sequential solving of simpler problems, with an approximated mathematical solution. Subsequently, when the simpler parts are assembled, they lead for a global problem's solution. This achievement is of extreme importance since the main problems to be addressed in engineering are complex and cannot be easily described with analytical methods.

Additionally, it has been observed an exponential progress of the application of FEM in complex engineering problems which is intrinsically connected to the increasing technological and calculus capacity of digital components in the past years [32].

Nowadays, the FEM is transversal to diverse fields of knowledge: vibration system studies, resolution of heat transfer, mechanical fluids, electrical and magnetic problems, material behaviour study, etc. The latter evolves a considerable range of behaviours such as linear elasticity (Hooke's law), plasticity, viscoplasticity, hiperelasticity, termoelasticity, etc.

4.1.3 Non-linearities

In FEM, the structures may be categorized based on three types of loading conditions [32]:

- *Static*: the load does not change in time or the time that the load is applied is big enough to not allow any considerable acceleration effects;
- *Quasistatic*: the load varies in time but still does not developed a dynamic behaviour, as in the case of a loading cycle time of low frequency;
- *Dynamic*: when the frequency of the loads is significant, their inertial effect on the structures can no longer be neglected.

As a first approach of any engineering problem, it is normally assumed a linear analysis. The following equation would then be valid for a structural problem:

$$\mathbf{F}=\mathbf{K}\mathbf{u}, \tag{4.1}$$

where $\mathbf{F}$ is the applied load vector, $\mathbf{U}$ is the displacement response and $\mathbf{K}$ is the stiffness matrix. The linear response can be demonstrated if a new load $\alpha\mathbf{F}$ is applied, where α is a constant, with the resulting values of displacement turning out to be $\alpha\mathbf{u}$. Nevertheless, these assumptions must be taken when employing this set of conditions [32]:

- The displacements of finite element assemblage are infinitesimally small;
- The material must shown linear elastic behaviour;

- The nature of boundary conditions remains unchanged during the application of the loads to the finite element assemblage.

Once the equilibrium of the equation 4.1 is not verified, the problem becomes non-linear.

Fortunately, in very specific conditions, a linear assumption may be given to certain physical systems and obtain feasible results. However, the majority of engineering problems depart from that condition [30]. In structural mechanics, a nonlinearity is verified when the relation $\mathbf{F} \neq \mathbf{Ku}$ occur. All forming processes, particularly sheet metal forming and tube hydroforming, represent a physical event where nonlinear behaviour is observed. The nonlinearity of a phenomenon is influenced for several aspects between tool and workpiece, as instance of material's plasticity, large displacements, great rotations, contact effects, etc. In order to separate the aspects refereed, nonlinearities are commonly divided into three groups: geometrical, material and contact [32]. The type of nonlinearities will be briefly discussed in the paragraphs below.

4.1.3.1 Geometric nonlinearity

The occurrence of this type of nonlinearities are originated by large deformations, displacements and/or rotations. This means that deformation and displacement cannot be described linearly. Bearing this in mind, it is important to adopt nonlinear physical quantities, such true strain and Cauchy stress tensors, alternatively to the engineering strain and stress which are considered inappropriate for geometric variations [32]. Once the deformation becomes large enough, the equilibrium equations must be written with respect to the deformed structural geometry because those equations were based on the original geometry of the structure, and the structure's geometry may suffer considerable modifications [30].

4.1.3.2 Material nonlinearity

Generically, the nonlinearity of the material is associated with phenomena such as nonlinear elasticity, plasticity and creep. For elastoplastic materials, a nonlinear relation begins when the yield surface reaches its own limit. From that point on, and as mentioned in the previous chapter, the material can suffer hardening effects as plastic strains are developed.

4.1.3.3 Contact nonlinearity

The boundary conditions vary along the process in quasistatic form (stamping and other metal forming technologies) or in dynamic form (structural impact or ballistic). Nonlinearities of this type are mainly influenced by two conditions: contact and friction. Typically, the contact condition involves the definition of impenetrability between geometric identities. The contact interactions of the geometric identities may be defined as rigid - deformable or deformable - deformable. On the other hand, the existence of friction is commonly modelled based in Coulomb's law, which describes the transmission of shear stress among the surfaces in contact. Commonly verified in numerical analysis of technological processes, the modelling of contact and friction conditions is typically a complex task. The interaction between contact surfaces origins an energy dissipation phenomena in form of heat and abrasion, which leads to an additional consideration of thermomechanical situation associated to the superficial interaction [32].

4.1.4 Type of elements

Regarding the dimensional nature of the problem to be simulated (1D, 2D, or 3D), different configurations of elements must be adopted. For certain engineering problems, the use of three-dimensional elements is mostly inevitable due to the geometrical environment where that problem is defined. As mentioned by Teixeira-Dias *et al* [32], the need of 3D type of elements is justified when the following conditions are met:

- The used materials require distinct mechanical properties relative to the three principal directions;
- The nodal boundary conditions are applied in three or more distinct planes;
- Nodal values of the variables to calculate require non-coplanar calculations, i.e. to be distinct in the three directions;
- The conjugation of previous two or more previous reasons.

These types of structural element can be categorized in two particular groups: solid elements and plate/shell elements that will be summarized in the following. Nevertheless, since fluid finite elements are also applied in the current work simulations, a brief description is also given.

4.1.4.1 Plate and shell elements

For structures where one of the dimension is substantially lower to the remaining dimensions, the use of this type of elements is appealing. Plates are indicated to model structures such as metallic panels, whereas shells may describe curved structures such tubes, pipes, pressure vessels, among others. The formulation related to plate/shell elements can be derived from degeneration of the solid elements. These modifications consist in transformations based purely on the field of displacements, wherein geometrical and cinematic simplifications are applied. Therefore, computational effort reduction is achieved compared to the solid elements.

Nevertheless, a few considerations must be taken into account towards plate/shell formulations. Once the deformation energy associated to the normal stresses of the element's surface is neglected, a condition of plane stress is invoked. For the case of conventional shells, the strain along the thickness direction results only from the Poisson's effect. For this reason, the shell elements were not chosen to discretize the tube in the current work's simulations.

4.1.4.2 Solid elements

The most frequent configurations of solid elements are the hexahedral and tetrahedral topologies. The use of hexahedral elements allows a superior modelling of realistic problems which involves loads, boundary conditions and properties of materials with a complex definition. Tetrahedral elements prove to be advantageous to describe complex geometries or to be use in free or unstructured refinement procedures. As previously mentioned, in order to obtain feasible results, the generated mesh must be refined to a certain extent which may result in high space and processing time costs in some situations.

Additionally, three-dimensional elements may present "locking" phenomena. These phenomena are characterized by an unphysically stiff response of the calculated deformation. "Locking" behaviours of solid elements may be categorized in two types: shear locking and volumetric locking. Shear locking occurs in first-order, fully integrated elements when subjected to bending, particularly for lower thickness values. On the other hand, volumetric locking occurs in fully integrated elements when the material behaviour is defined as (or almost) incompressible. Both problems may be alleviated locking by refining the mesh in regions of large plastic strain [35].

4.1.4.3 Fluid elements

The fluid elements used in this work are F3D3 and F3D4, available in Abaqus library. At the first sight they might be mistaken as surface elements, but they are actually volume elements when accounted for the cavity node reference, as shown in Figure 4.1. The cavity node is where the global pressure is assigned. If the pressure value is defined, the fluid will automatically adjust it's volume to fill the cavity, simulating the entering or leaving of the fluid regarding the actual conditions. If not prescribed, the fluid is admitted as sealed and it's pressure will depend on the boundary conditions [35].

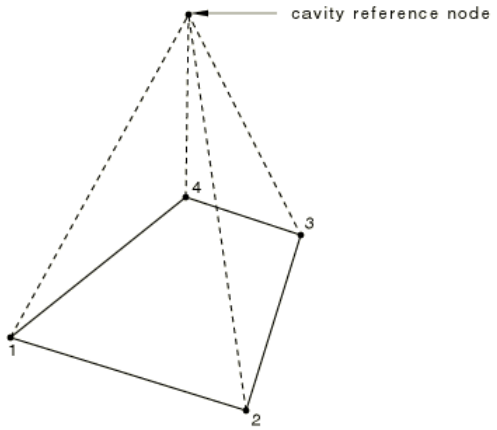

Figure 4.1: Hydrostatic F3D4 fluid element scheme [35].

4.2 FEM and THF research

4.2.1 Overview

Through the last decades, the design for hydroforming or even conventional forming processes was based on past experience and iterative "trial-and-error" methods which proved to be tremendously time consuming as well expensive. The development of numerical simulation tools based on FEM received a significantly growth in a wide range of industrial applications, as it is the case of the process in focus. Promoting the study of arbitrary combinations of input parameters, including design parameters and process conditions to be investigated, numerical simulations can reduce the developing time and the prototyping cost [36].

Tekkaya [37] identified the overall industrial goals for forming simulations and organized them in the following groups:

- *Time reduction:* early checking of producibility of workpieces, reduction of the development times, reduction of the try-out-times, quick response to modification wishes;
- *Cost Reduction:* cheaper products, reduction of die costs, press down sizing and increase of reliability;
- *Increase of product quality:* optimal selection of the workpiece material, production of more complicated parts, know-how accumulation for new materials, process repeatability and optimization.

From the software that have emerged and have been used for simulation of the hydroforming processes, LS-DYNA, Abaqus, PAM-STAMP and MARC are the most popular.

4.2.2 Abaqus software

Once Abaqus is the FEM commercial software used to carry out the current work, it is reasonable to briefly explain how it is organized. Mainly, Abaqus consists in three core products of analysis: Abaqus/Standard, Abaqus/Explicit and Abaqus CFD [38]. The analysis core used in the present work is Abaqus/Standard, since it provides linear and non-linear implicit formulations for static or quasistatic problems. In opposition, Abaqus/Explicit is indicated to modelling brief, transient dynamic events such as blast or impact problems. Lastly, Abaqus/CFD is suitable for dynamic problems involving fluids.

Abaqus/CAE represents a complete Abaqus environment which is responsible for the pre and postprocessing. The pre-processing stage corresponds to the stage where it is defined all the relevant aspects of the model before being submitted to analysis. Basically, the pre-processor is responsible to generate an input file which contains information regarding the part with a geometry, material properties, boundary and loading conditions defined in the Abaqus/CAE environment. Due to practical purposes, the user may change manually this file with a text editor. Abaqus/Viewer is a subset of Abaqus/CAE and corresponds to the post-processor. Therefore, it provides graphical display of the finite element models and results.

4.2.3 Research in THF

When confronted with the limitations of theoretical analysis and experimental studies, it is easy to understand the vital role that numerical simulations occupy in the development of the process design and execution. Researchers can investigated the effects of material properties, geometrical factors, process parameters and friction by varying these parameters in a controlled environment.

For instance, the effects on the pre-forming stage to obtain "useful" wrinkles were studied by Lang *et al.* for a bulge tube, by admitting that not all wrinkles were harmful to forming process [15]. In pre-forming stage, different internal pressure and axial feeding sets were applied based on a multi-step variation method. This proved to be more effective in controlling the wavy wrinkles formation, in comparison with a linear variation

method. Consequently, those wrinkles would be dissipated in the calibration stage, where high pressure is applied. In a consequent research work [13], Lang *et al.* extended the investigation by differentiating the pre-forming stage (with a pre-forming die cavity) and the calibration stage (with a die cavity) with the final form. Two designs of pre-forming dies were used (25°and 45°), where the the designed 25°pre-forming die proved to be better in successfully creating useful uniform wrinkles. Both works were in agreement with the respective numerical and experimental tests.

In order to accurately predict the instabilities occurrence, damage models and fracture criteria may be added to the analysis. On their research work, Sornin *et al.* [39] highlighted the interest of continuum damage modelling for the formability and final part load carrying capacity prediction of T and Y-shaped tubes. A modified maximum force criterion was used to predict the location of possible defects. To overcome an eventual failure of the crack propagation detection, a continuum damage model was implemented accounting to the pressure sign and stress triaxiality threshold. Thus, the detection of critical zones regarding the damage effect initiation and growing is allowed.

As a neglected part of numerical simulations, some researchers started to take into account the weld seam properties to evaluate its influence in the forming models. In 2004, Kim *et al.* [40] considered relevant to evaluate the influence of the weld metal properties on the forming limit of bulge forming, since no previous study on the subject was found. By modelling the weld metal, HAZ and based metal respective material properties, it was concluded that this approach was more realistic in comparison to representing the tube by only the weld metal zone or even by neglecting the weld bead. Using a ductile bursting criterion, it was observed that fracture would start on the HAZ, as it is demonstrated in Figure 4.2.

Khalfallah [41] proposed a simple method to accurately determine the mechanical properties of weld bead and HAZ regions in seamed tubes. The approach consisted in combining the rule of mixtures with the standard tensile test properties and the microhardness measurements. The results obtained from numerical simulations by FEM and experimental tests were found to be in good agreement based on the evaluation of the thickness in axial direction.

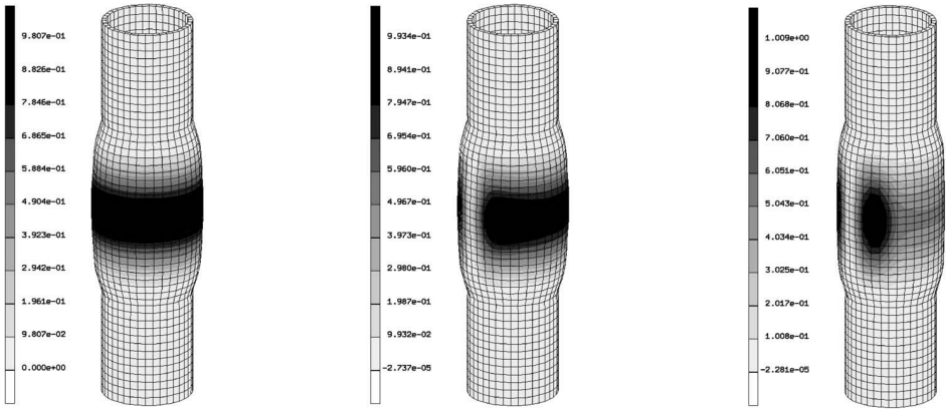

(a) No weld (b) Weld seam (c) Weld seam and HAZ

Figure 4.2: Distribution of the ductile fracture prediction values on bulge models with different material region properties defined [40]

On the other hand, more complex parts require bending and/or crushing processes before the hydrofoming stage. For a proper tube hydroforming analysis, it is necessary to include the results of the stress and strain history resulting of the pre-forming stage analysis. So far, the FEM is the only way to achieve this in pursuance of a more realistic forming of complex parts [5]. For instance, Oliveira *et al* [42] examined the effects of the tube bending and hydroforming processes on the characteristics of aluminium alloy S-rail used in crash applications, applying the procedure previously described to guarantee a more feasible analysis, as shown in Figure 4.3.

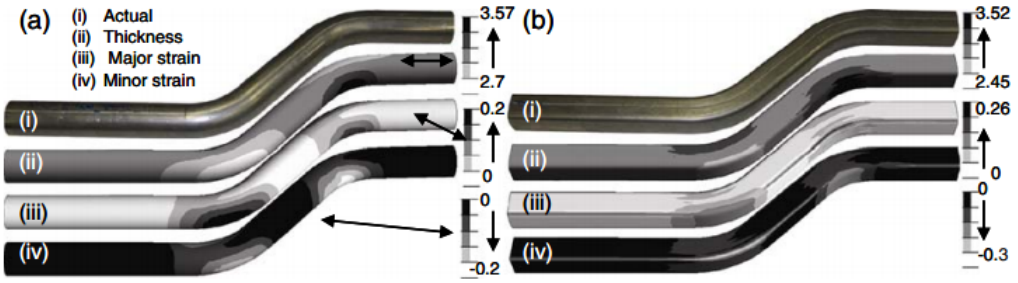

Figure 4.3: S-rails: (a) Non-hydroformed and (b) hydroformed, where: (i) the actual geometry, and (ii) predicted thickness; (iii) predicted major strain and (iv) minor strain [42].

Finally, another major advantages of using FEM in THF is the possibility of implement controlled analysis techniques in numerical simulations to calculate the optimized loading paths. As presented by Gosh *et al.* [14], in order to provide a faster and systematic approach of the loading paths, the following strategies can be choosen:

- *Trial and Error FEA Simulation approach* - which simply applies the trial and error strategies using iterative finite element simulation until acceptable forming are achieved. To reduce the loading paths calculation time, it is also used a self-feeding technique which consist on carrying out simulations without forced axial feeding to provide the initial loading path;

- *Optimization approach* - simulations are carried out repetitively until an optimal loading path is obtained based on formulations of an objective and constraints functions, towards an optimizing tube-wall thickness distribution;

- *Adaptive approach* - based on a control strategy, it monitors the failure modes of wrinkling and bursting as indicators to adjust the loading paths in simulation by feedback control. It determines the process-loading curve by running a single simulation, which comparatively to the previous methods, the adaptive approach reveals to be faster;

- *Fuzzy Load Control* - Fuzzy Load Control involves development of fuzzy logic rules supported by previous knowledge of THF process. The failure indicators for wrinkling and buckling thresholds are stipulated by those rules, the main difference from the adaptive approach.

Chapter 5

Bulge benchmark

Summary In tubular hydroforming research, a bulge benchmark presents a common choice in literature due to its simplicity and easy reproducibility both in experimental an numerical testing. For that reason, the benchmark is included in this work as first test case. This chapter is devoted to the analysis of three main models. In the first one, the tube's material is an aluminum alloy. For the second and third model is chosen an low carbon steel, while in the latter a weld seam is included. Thickness variation, strain and stress behaviour, instability appearances and the weld seam influence are the features aimed to be discussed and evaluated at the end of the chapter.

5.1 Model description

The bulge-shaped part is a well-known and one of the most used case study to carry out tubular hydroforming experiences. The current model is based on the bulge axissymetric geometry used by Ahmetoglu *et al.* in its research [43]. The current models are defined in three parts: die, tube and fluid as shown in Figure 5.1. The die geometry is shown in figure 5.2, as well as the initial tube geometry. The modelled die is fully meshed by three dimensional 4-noded elements (R3D4). The tube's mesh is made with 8-noded hexahedral elements (C3D8). The fluid part is defined by three-dimensional 4-noded fluid elements (F3D4) at the surface which contacts with the tube's inner surface, and three dimensional 3-noded fluid elements (F3D3) at the extremities. The fluid is defined incompressible or approximately incompressible. Also, the fluid pressure is set in a single node which defines the whole fluid cavity. Instead of a double axial feeding, the current model only have a moving punch side. To simulate the punch stroke, displacement was directly defined in the tube and fluid nodes, in alternative to include a rigid body component for the effect.

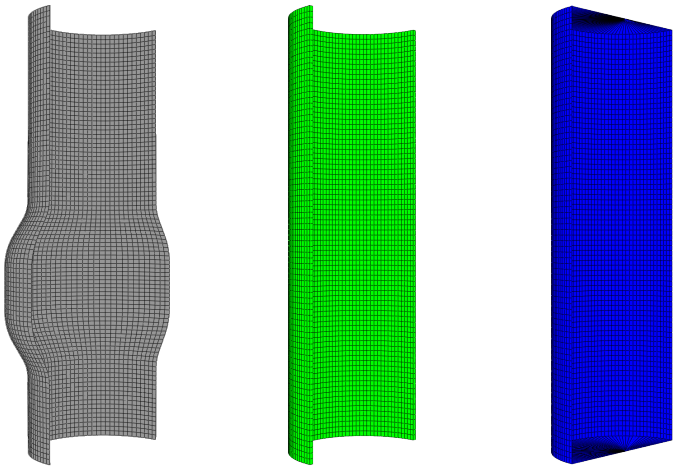

(a) (b) (c)

Figure 5.1: Schematic representation of the axissymetric model simulation components: a) Die b) Tube and c) Fluid.

As mentioned before, the main software used was Abaqus, although Femap was adopted at the first stages of pre-processing due practical purposes. The simulations were carried out in static analysis, in implicit form, including geometric and material non-linearities as well as mechanical contact formulation. The contact between the die and the tube's outside surface was considered to be frictionless.

In order to be coherent and systematic through models, the one half model design was adopted since it is the simpler case of symmetry when a weld bead is included. Additionally, it requires less computational effort, not only reducing the computer processing time but also memory space, when compared with the complete model design.

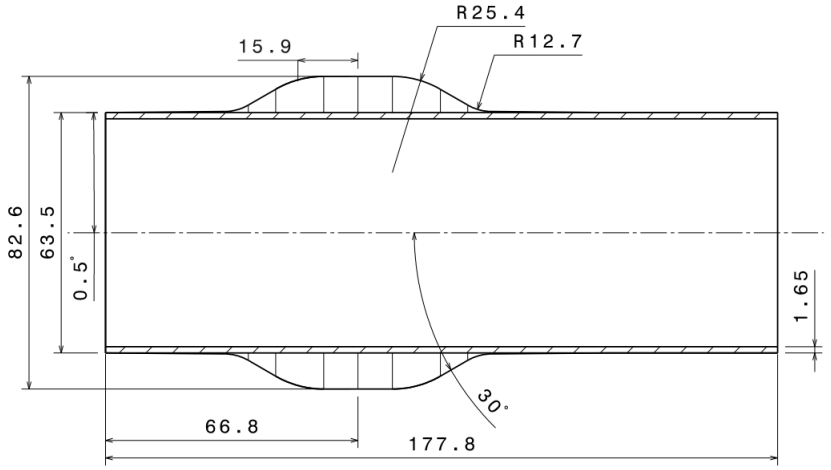

Figure 5.2: Bulge die and tube geometry (measured in mm).

5.2 Seamless tubes

In order to simulate extruded tubes, i.e. free weld bead tubes, it is presented a couple of simulations. Between those, it was used two types of materials and different mesh set, with different number of elements. Basically, a sensitivity analysis of mesh refinement is conducted to provide better insight of its influence in the numerical results of this nature.

5.2.1 AA6061-T6 tube set

The benchmark approached uses as base material the aluminium alloy mentioned in this subsection. The material's mechanical properties defined in Abaqus are indicated in table 5.1.

Table 5.1: Properties of aluminium alloy 6061-T6 by Ahmetoglu *et al.* [43].

Geometry and elastic properties	
Thickness	t=1.65 mm
Outside diameter	OD=63.5 mm
Young's Modulus	E = 70 GPa
Poisson's ratio	ν =0.3
Plastic properties	
Strain	Stress (MPa)
0.0000	272
0.0154	276
0.0178	279.9
0.0610	319
0.1130	341.5
0.1250	338.7

As already mentioned, it is conducted a couple of simulations with different mesh sets of the tube, which also influences directly the element's number of the fluid component. This mesh refinement is made in the following way: 4800, 9600 and 14400 elements respectively. More precisely, 60 elements in circumferential direction and 80 elements in axial direction, although varying in radial direction by a factor of 1, 2 and 3. The mesh set is uniform along the tube, which means there is no particular refined zone. In all simulations, the die's mesh is kept constant for uniformity and easier perception purposes.

The respective load paths applied during numerical simulations are indicated in Figure 5.3. For an ideal comparison, the same loading path was defined for each model. Unfortunately, that specification is not verified for all models since convergence problems were experienced - a common problem when numerical simulations are run in the implicit form. By this means, in order to conclude some of the simulations, loading paths had to be re-adjusted with the minimum changes possible. Also, these loading paths were initially based on the ones presented by Roque [44] as guidelines for the cases which were used AA6061-T6 tubes. As can be checked in Figure 5.3, the loading path for the model

with only 1 element through thickness (1 layer) is completely defined in 5 steps, instead of 7 steps as it is the case of the remaining simulations with 2 and 3 elements through thickness (2 and 3 layers). Both final pressure and final axial feeding are equal to both graphs. Following Roque's consideration, the pressure and axial feeding where given in alternative steps: odd steps as pressure steps and even steps for axial feeding steps.

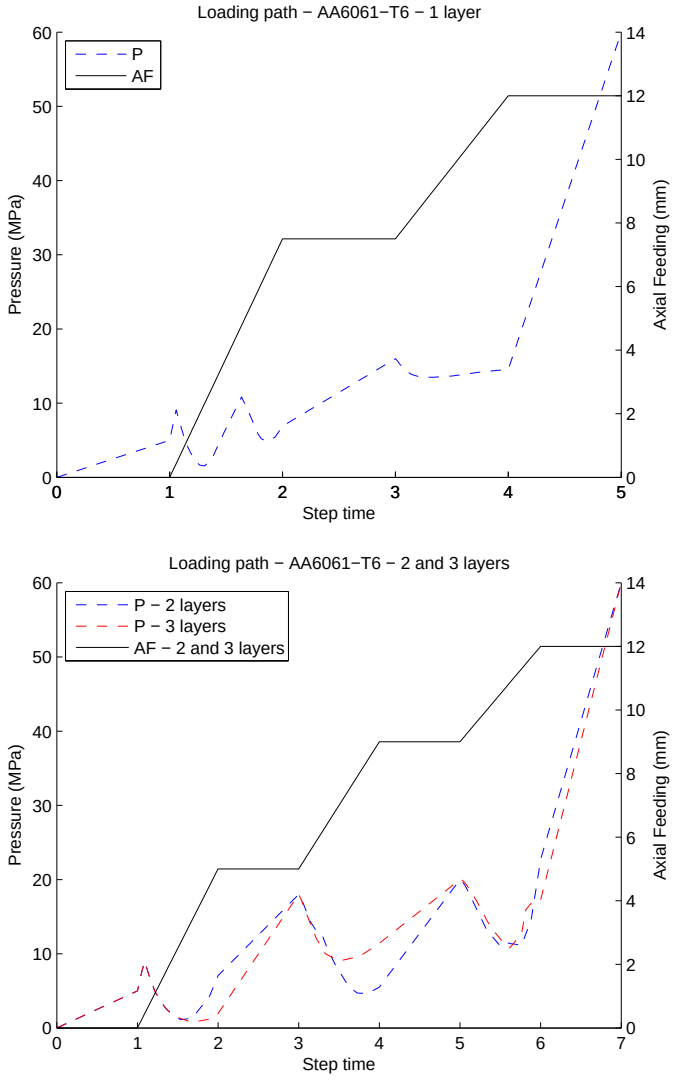

Figure 5.3: Loading paths of AA6061-T6 axissymetric tubes.

It is important to have in consideration that no optimization study was conducted to obtain the ideal loading paths. Instead, loading path curves were based on assumptions with trial-error attempts until simulations were acceptable for comparison purposes. A general display of the stress and strains induced on the tube is given in tables 5.2 and 5.3, each one with respective legend.

Table 5.2: Von Mises stress in AA6061-T6 axissymetric models - Inside view.

Step	1 layer	2 layers	3 layers
1	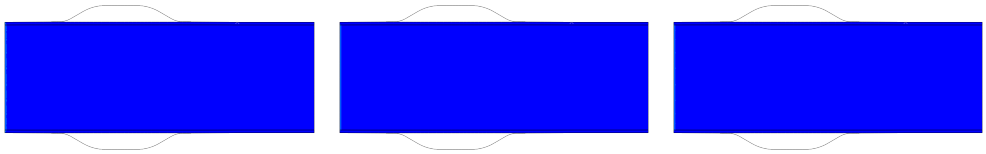		
2	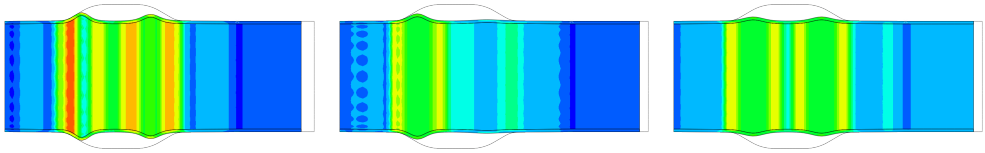		
3	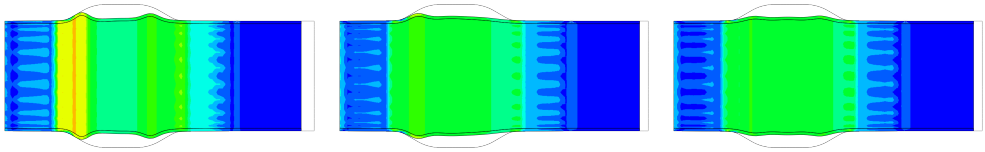		
4	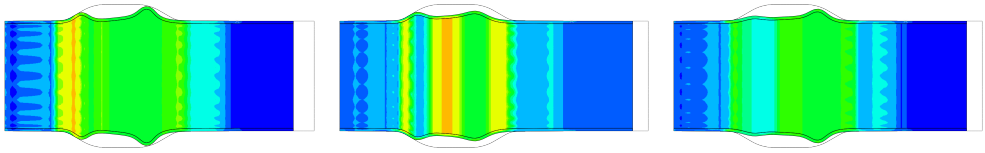		
5	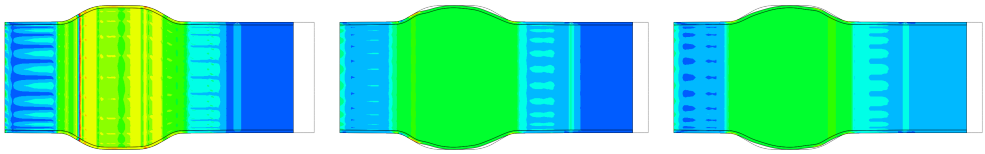		
6	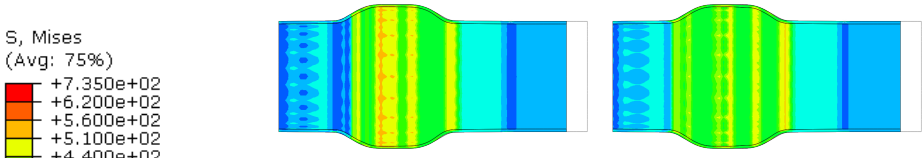		
7	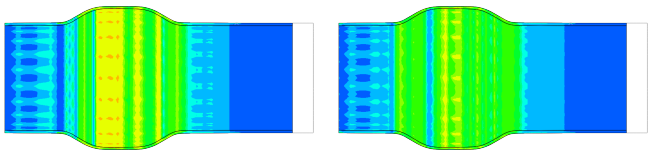		

Table 5.3: Equivalent plastic strain levels (PEEQ) in AA6061-T6 axissymetric models - inside view

Step	1 layer	2 layers	3 layers
1	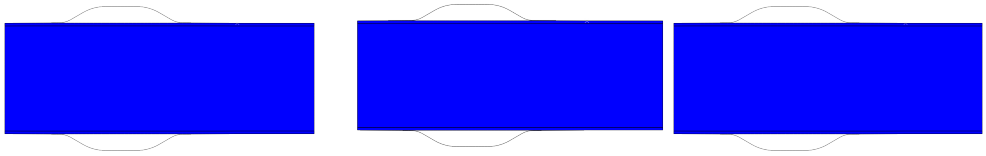		
2	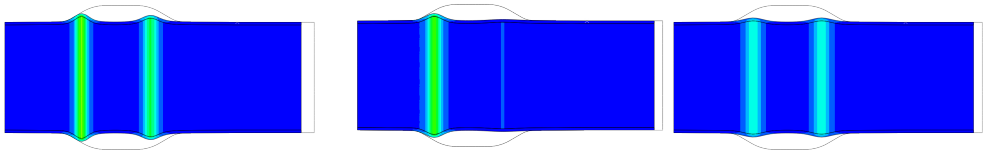		
3	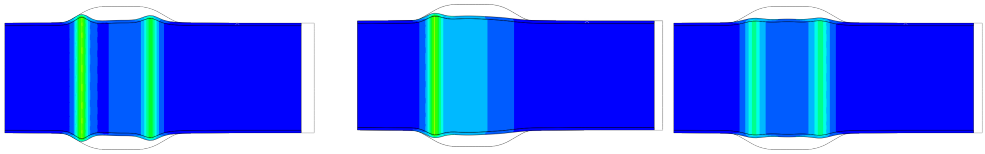		
4	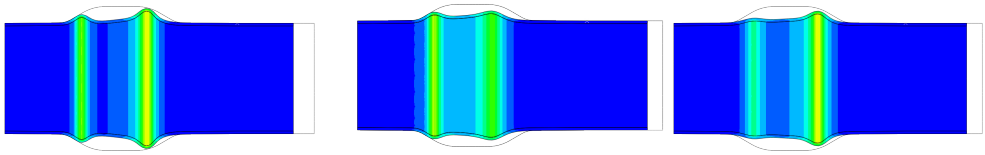		
5	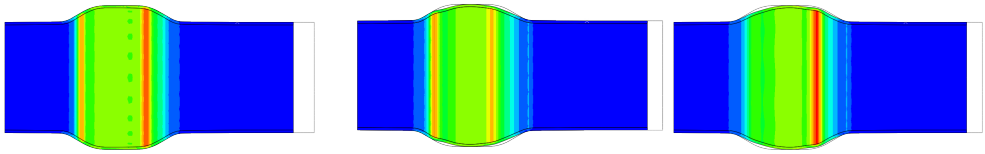		
6	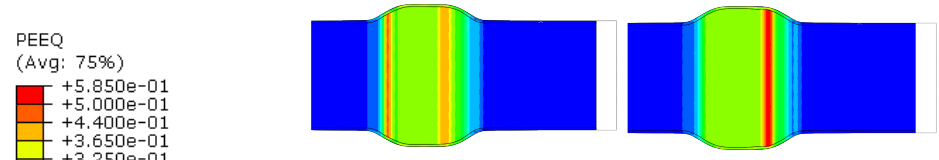		
7	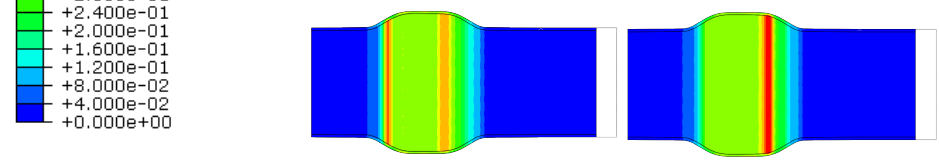		

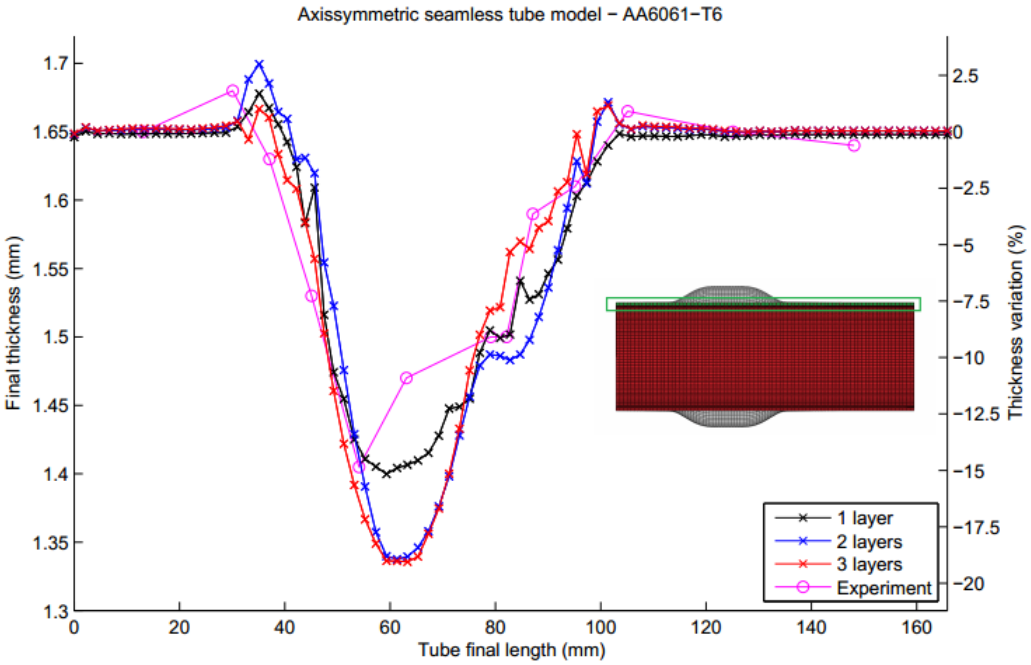

Figure 5.4: Final thickness and its variation of AA6061-T6 axissymmetric models and the result experimentally obtained by Ahmetoglu [43] along the tube length (green).

Due the axissymetric conditions, the thickness may be evaluated longitudinally as demonstrated in Figure 5.4. The final thickness and the corresponding variation of the model sets are represent, as well as the experimental thickness results of Ahmetoglu [43], for comparison purposes. The main variations are located in the bulge zone, where the refined 2 and 3 layers models shown a higher necking compared to the remaining models. This outcome may have been affected by the additional steps required to form the final geometry specified.

5.2.2 S235JR tube set

The previous simulations were repeated, now considering a low carbon steel S235JR, whose properties can be found in Figure 5.5. Only the parent material was used, since the models of the section do not considered the weld bead existence. Although, the graph of S235JR material properties also shown its mechanical properties in the weld bead and heat affected zone (HAZ), which are approached in a following subsection. Besides the material, every parameter associated with the workpiece in the numerical environment was kept identical.

However, the process parameters had to be adjusted to the new material, as example of the loading paths. For this set of models, a common set of axial feeding and internal pressure conditions was shared as may be visualized in Figure 5.6, i.e there is no variation in the number of the steps as it was demonstrated in the previous set. The color mapped tube section images representing the stress and strain distribution along the steps are shown in tables 5.4 and 5.5. The associated legend is in figure 5.7. The final thickness graph along the tube length is shown in figure 5.8, where the thickness variations among

models are less accentuated comparatively to the results of the previous set.

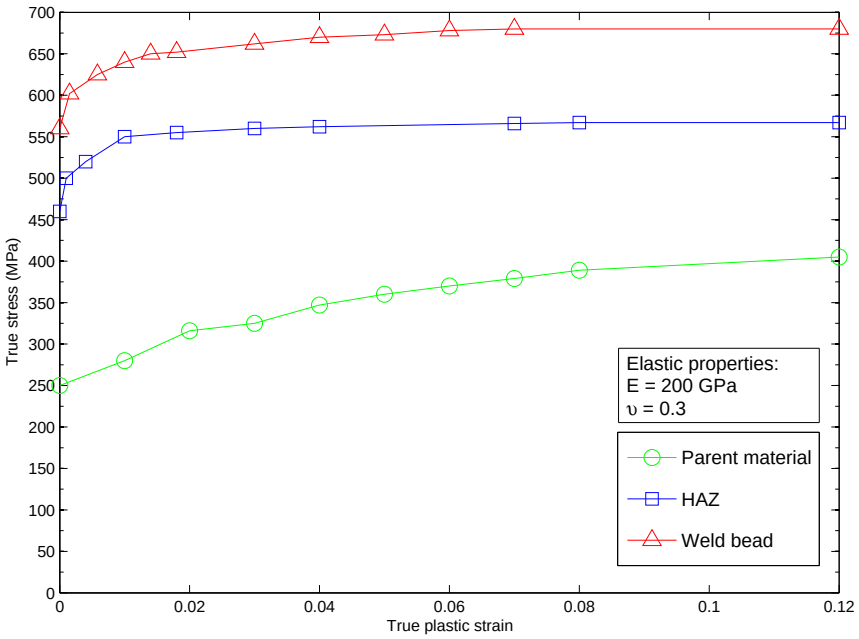

Figure 5.5: Elastic and plastic mechanical properties of the different regions of the welded material adapted from Khalfallah [41].

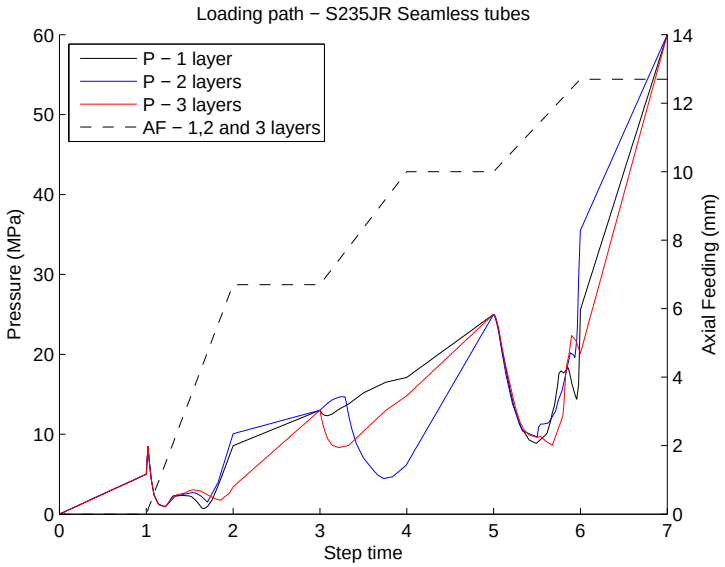

Figure 5.6: Loading paths of S235JR axissymetric seamless tubes.

Table 5.4: Von Mises stress in S235JR axissymetric seamless models - inside view

Step	1 layer	2 layers	3 layers
1	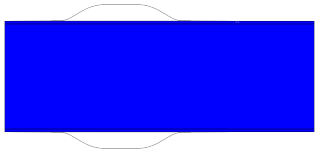	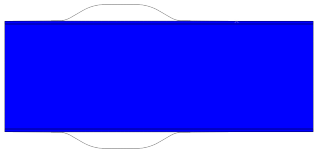	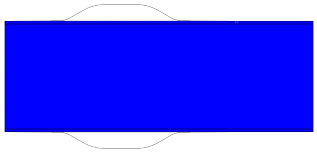
2	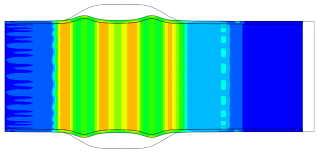	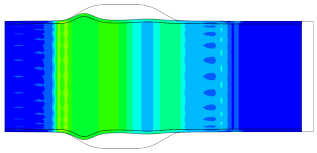	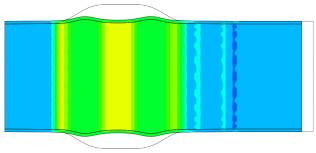
3	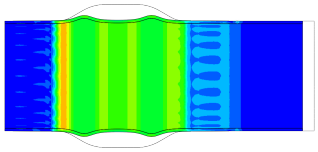	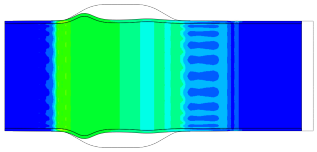	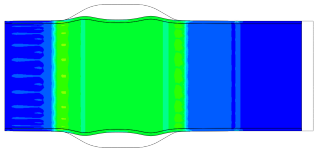
4	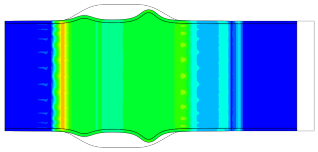	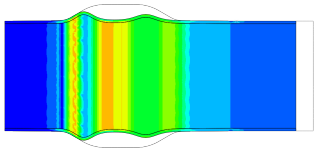	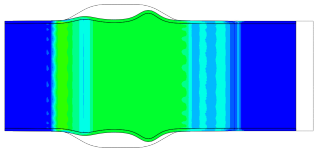
5	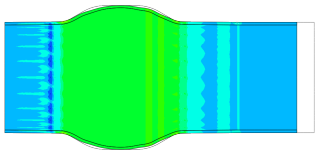	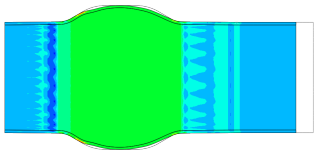	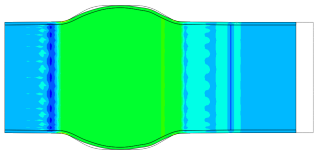
6	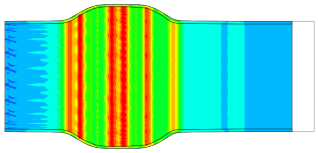	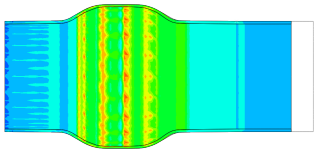	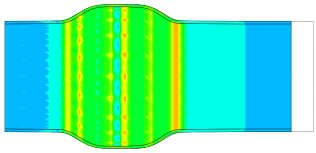
7	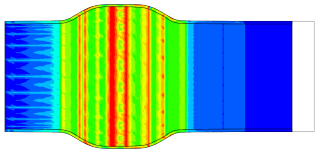	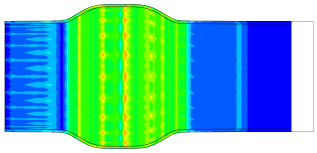	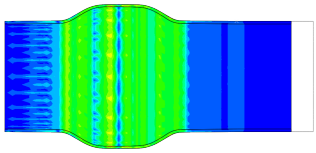

Table 5.5: PEEQ in S235JR axissymetric seamless models - inside view.

Step	1 layer	2 layers	3 layers
1	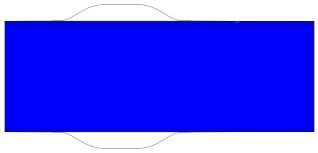	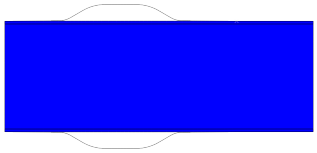	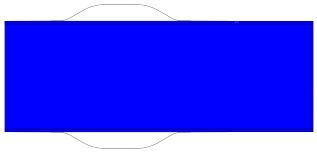
2	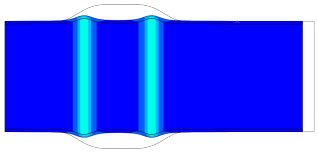	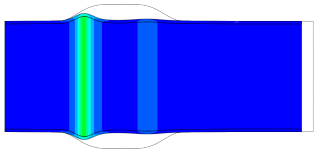	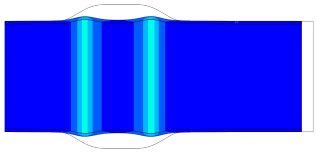
3	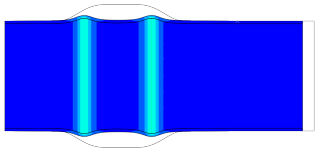	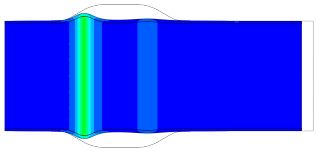	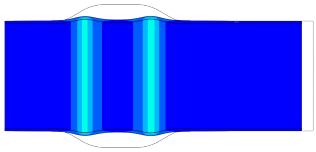
4	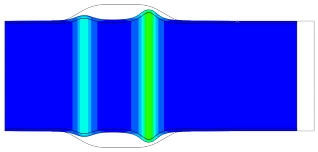	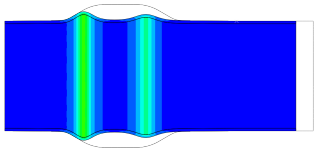	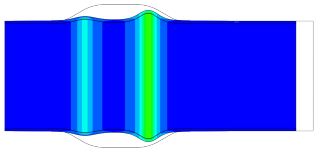
5	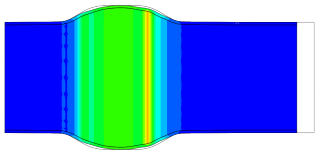	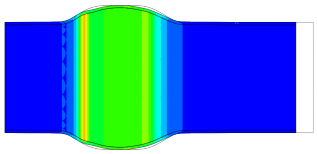	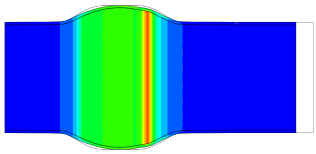
6	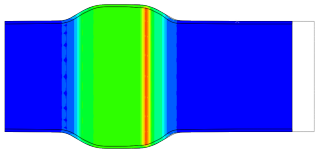	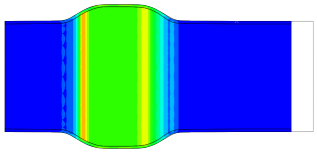	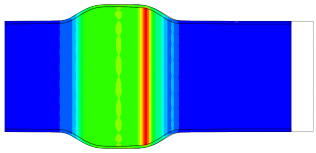
7	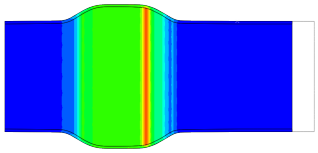	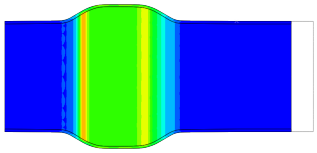	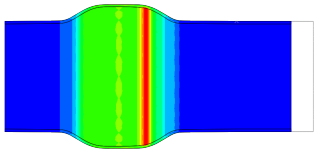

(a) Von Mises (b) PEEQ

Figure 5.7: Legend of the models in table 5.4 and 5.5

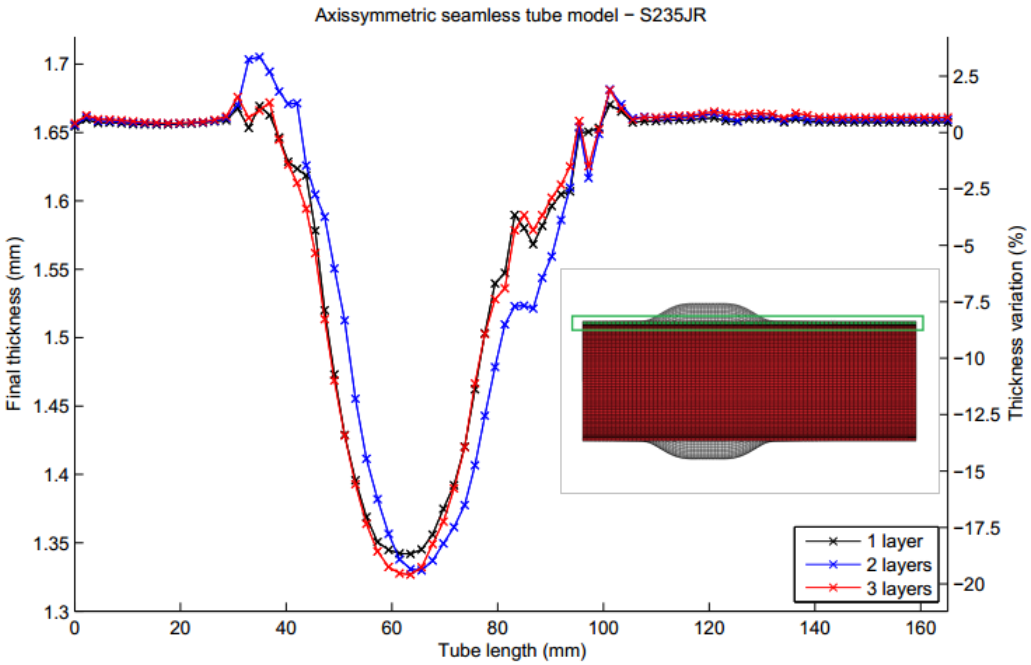

Figure 5.8: Final thickness and its variation of S235JR axissymmetric seamless models along the tube length (green).

5.3 Seamed tubes

The tubes modelled for this purpose are defined with a weld zone as shown in figure 5.9. This zone is composed by weld bead and the surrounding heat affected zone (HAZ). Khalfallah [41] used welded low carbon steel S235JR tubes with an outside diameter of 50 mm and a thickness of 1.2 mm. The weld zone dimensions of those tubes are 1 mm for the weld bead and 5 mm for the HAZ. Since the tube's dimensions from Khalfallah's experiments are quite similar to the dimensions of the tube used in this chapter, the same weld zone dimensions were assumed for present case.

In the simulation environment, weld zone was defined by 3 elements in circumferential

direction: 2 elements for the HAZ of 2 mm and 1 element for the weld bead of 0.5 mm, since it is located in the symmetry plane.

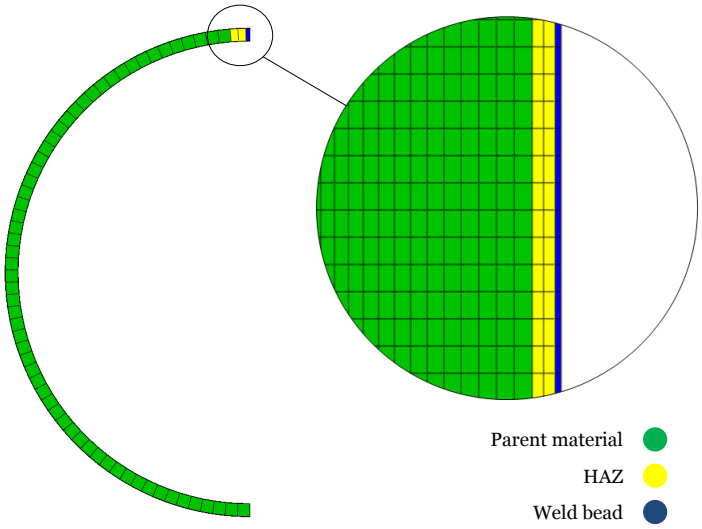

Figure 5.9: Scheme of the weld seam components.

The loading paths selected in the current subsection are not uniform among the simulations. As exihbited in figure 5.10, the 1 and 3 layers models share the same loading path but the axial feeding path had to be adjusted in step 4 for 2 layer model.

Identically to the previous subsection, the stress and strain color mapped images were also taken and organized in the Tables 5.6 and 5.7 with the final stages of each step.

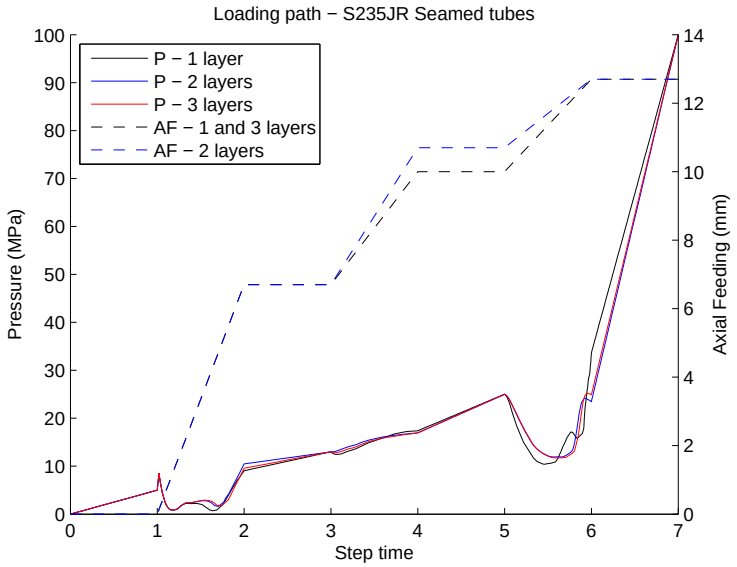

Figure 5.10: Loading paths of S235JR axissymetric seamled tubes.

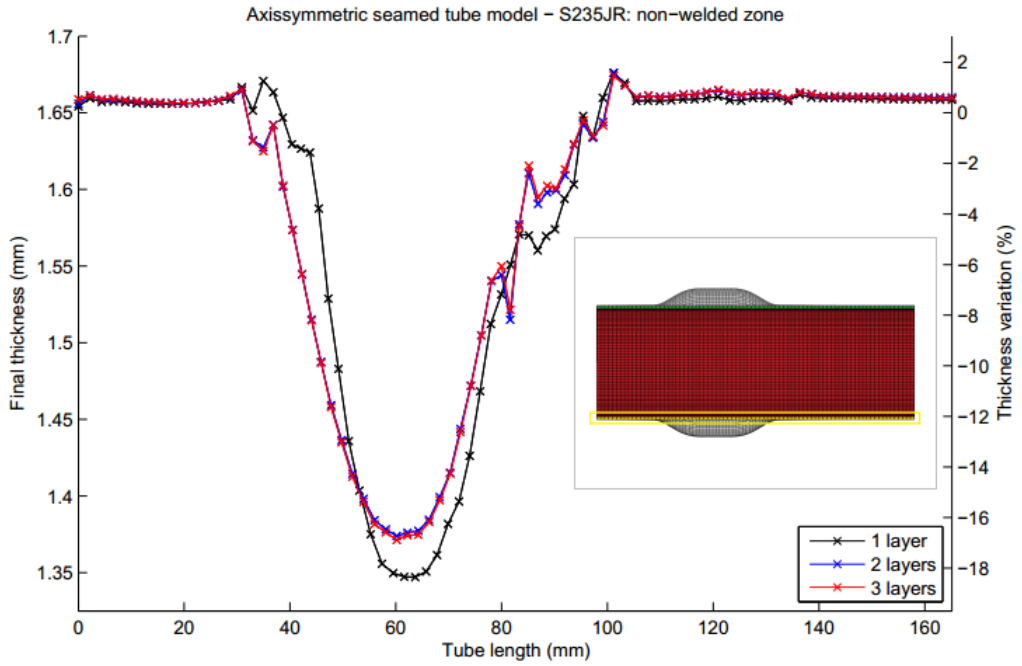

Figure 5.11: Final thickness and its variation of S235JR axissymmetric models - non-welded zone (yellow).

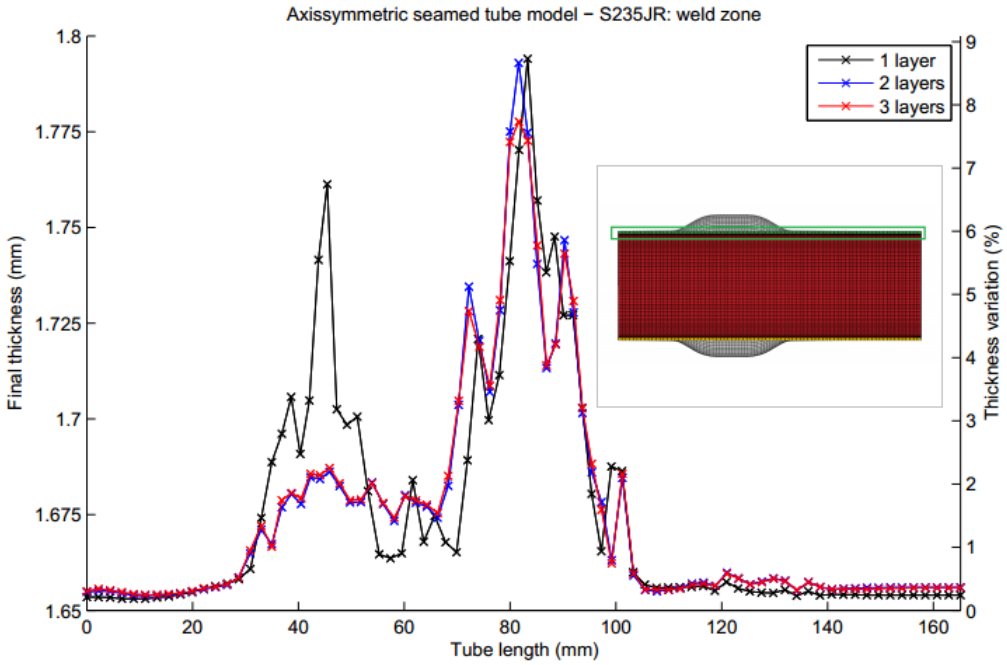

Figure 5.12: Final thickness and its variation of S235JR axissymmetric models - welded zone (green).

Table 5.6: Von Mises stress in S235JR axissymetric seamed models - inside view.

Step	1 layer	2 layers	3 layers
1	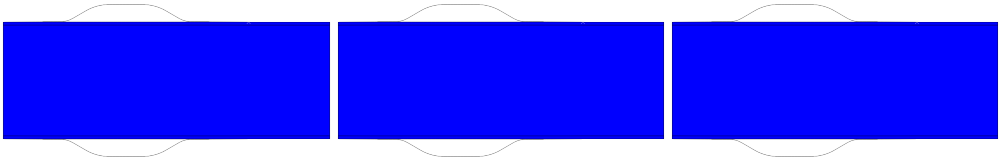		
2	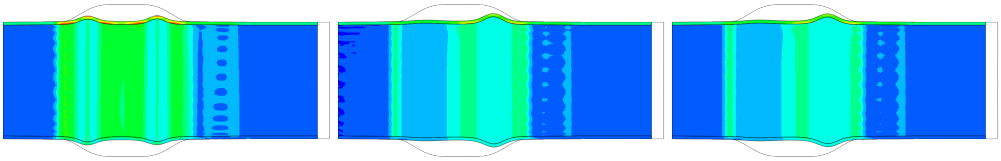		
3	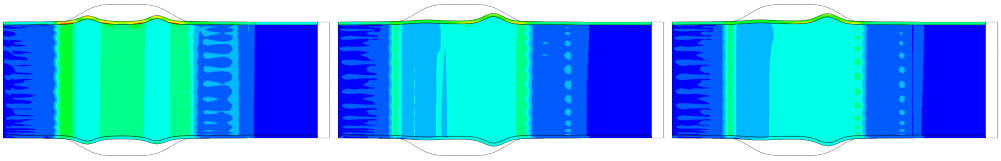		
4	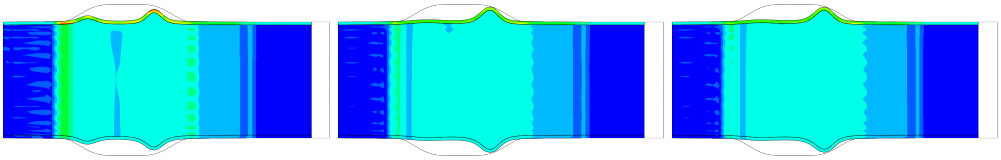		
5	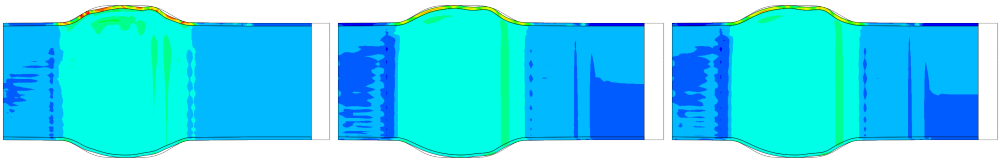		
6	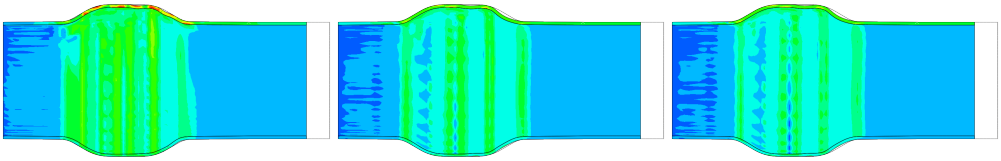		
7	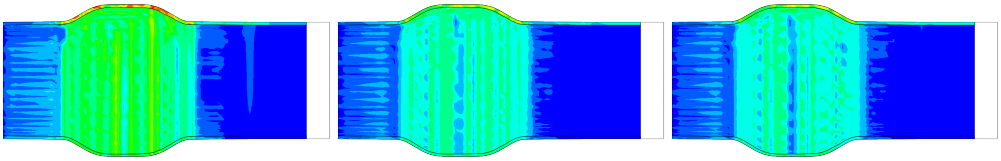		

Table 5.7: PEEQ in S235JR axissymetric seamed models - inside view.

Step	1 layer	2 layers	3 layers
1	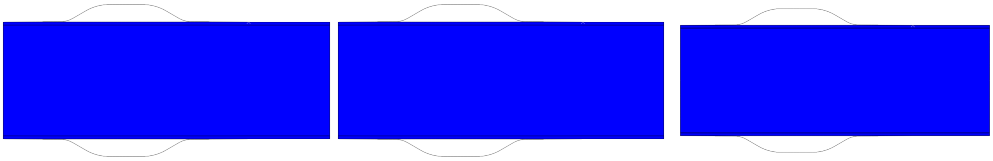		
2	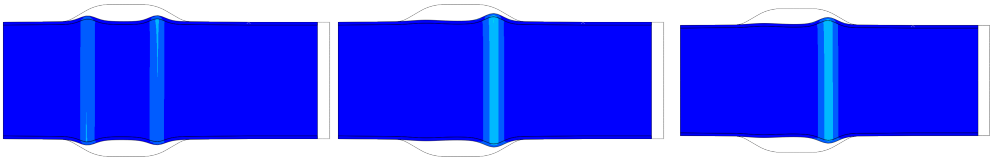		
3	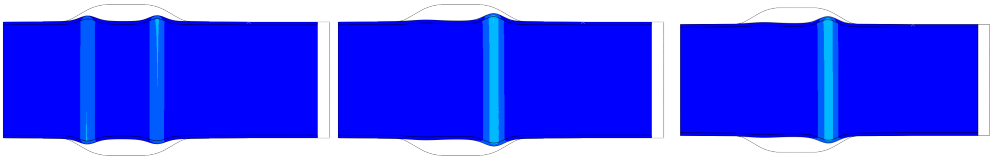		
4	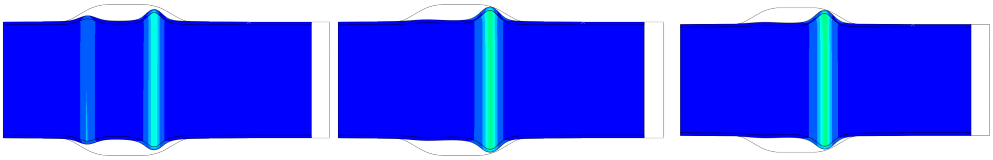		
5	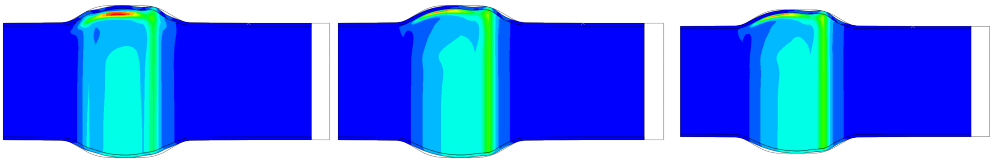		
6	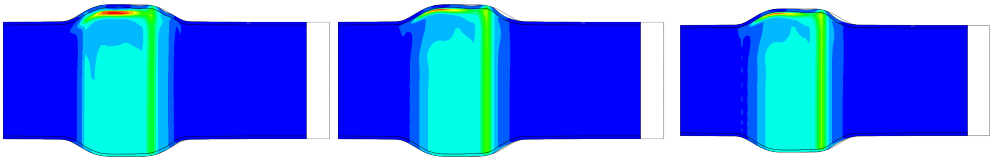		
7	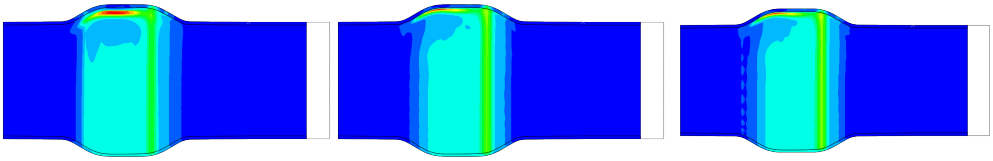		

(a) Von Mises (b) PEEQ

Figure 5.13: Legend of the models in Table 5.6 and 5.7.

Table 5.8: Localized strain in the S235JR welded tube set.

	Longitudinal cut view	Transversal cut view
	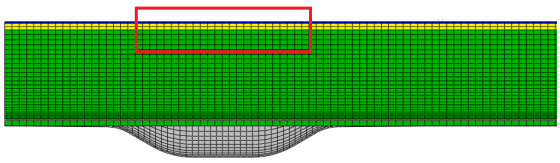	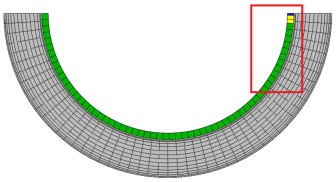
	Zoomed locations	
1 layer	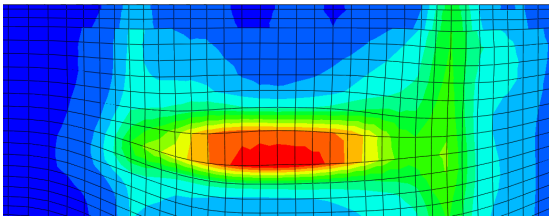	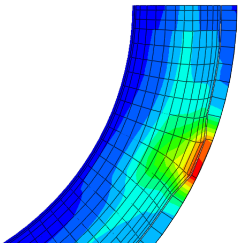
2 layers	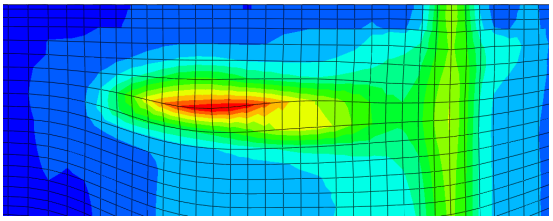	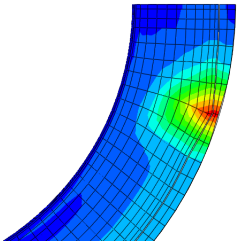
3 layers	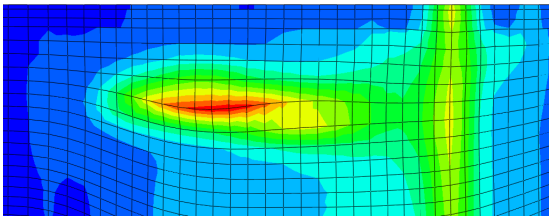	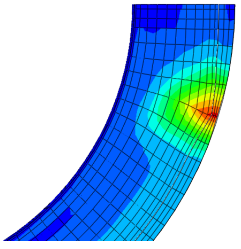

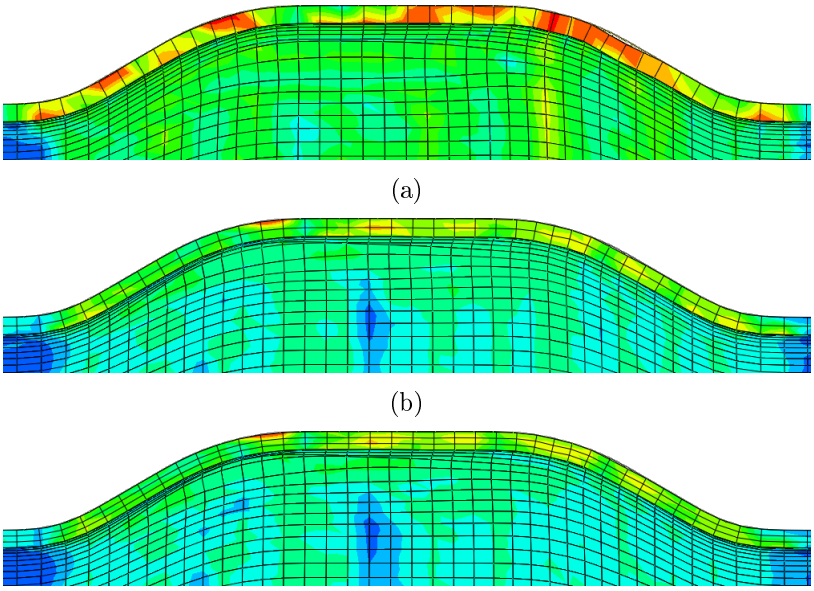

(a) (b) (c)

Figure 5.14: Von Mises stress distribution in the weld location: zoom from last step of the models on Table 5.6: a) 1 layer b) 2 layers c) 3 layers.

5.4 Analysis of results

In this chapter were presented 3 main numerical simulation sets for the study case of tube hydroforming: 2 seamless tube sets of different materials and a seamed tube set. For each set, 3 simulations models were made with different number of tube elements, in order to evaluate the sensitivity of the simulation set.

5.4.1 AA6061-T6 seamless tube set

Following a chronological criterion, the AA6061-T6 tube set is firstly discussed. Observing the progression in the different steps in Table 5.2, one can confirm that 1 layer model and 3 layers model have similar wrinkle formation, even with different amount of numerical steps.

Nevertheless, the stress levels in the forming stages of 1 layer model are higher. This situation is most likely to be caused by some volumetric locking effect due the low mesh refinement. In contrast, 2 and 3 layers models, which share the same loading paths, present an uneven wrinkle formation, which results also in a different stress and strain distributions. This suggests a certain level of sensitivity to the tube's mesh.

As expected, the most affected zones in terms of thickness variation are located in the wrinkle area. This fact is more obvious in the 3 layers model in Table 5.3, where the plastic strain evolution is displayed. All models presented a final thickness along the final tube length more or less identical to the experimental configuration. However, a marked thinning zone is verified for all the numerical simulations at the center of the bulge zone,

specially for 2 and 3 layers models. At the diameter transition zones, a slight thickening is generally observed. It becomes easy to infer from which side the axial feeding was applied, based on the thickness distribution. The material flow is higher near the punch side, resulting in a less thinned area. The second thinning peak is coincident with the wrinkle formed on the side of the axial punch.

5.4.2 S235JR seamless tube set

The material transition is performed to the given low carbon steel. Besides, a slight change was made in the final length of the loading path curve, from 12 to 12.7 mm, to guarantee a common loading path to each model as shown in figure 5.6. In early experiments, simulations with simultaneous pressure and axial feeding were conducted but the convergence rate was difficult to find. To decrease and simplify the loading path definition, the differentiate loading strategy used by Roque in his work [44] was also applied.

The pressure curve variations results of the fluid compression in the cavity during the punch displacement. Owing to the nearly incompressible state, sometimes defining a valid displacement was challenging since pressure values abruptly raised, representing a meaningless situation, physically. Taking into account the previous statements, no additional parameters were changed in order to minimize their influence in the results. Therefore, the same numerical simulations structure was driven.

In comparison with the AA6061-T6 set of models, the S235JR models configuration proved to be quite similar in the overall of the forming stages. The stress and strain distribution presented identical patterns too. The addition of more elements in thickness direction seems to influence the forming progression and stress distribution.

The wrinkle's disposition for the 1 and 3 layers models are in agreement along the steps. Two wrinkles are formed whereas the wrinkle from the side of the axial displacement is more accentuated. In contrast, the first stages of 2 layers model exhibits the forming of just one wrinkle, near the bulge wall which is most distant from the moving punch. The second wrinkle only appears along the fourth step. Similarly to the previous set, at the end, the plastic strain levels are more severe for the the wrinkle which had been more developed during the forming process, i.e. the right wrinkle for the 1 and 3 layer model and the left wrinkle for the 2 layers model according to Table 5.5. The stress levels proved to be higher in the 1 layer models than in the rest of the models, for the same reasons mentioned in the previous set.

The configuration of final thickness curves for the S235JR bulged tubes showed to be identical to the equivalent curves for the aluminium alloy models defined by 7 steps loading path. Both models presented a peak of approximately 19 - 20% thickness reduction in the bulge zone. The second graphic lump, at 85 mm, is coincident with the right wrinkle already discussed, although a few differences are noticed.

As previously mentioned, 1 and 3 layers model share a same tube forming path. This evidence is also clear in their final thickness, which reveals minimum variations. The discrepancy for the 2 layers final thickness curve may be justified by the mesh refinement that led to a different forming path. For instance, the presence of an early left wrinkle is noticed in the tube's thickening on the left transition zone of the die (35 mm). On the other hand, a slightly thinning is revealed at the right wrinkle location (85 mm) compared to the other simulations.

5.4.3 S235JR seamed tube set

Including a weld bead, which is often a neglected part in numerical models for simplification purposes, proved to lead to different results, as expected. The loading path curves set for the bulge seamed models is kept from the previous analysis, with a small change. The final pressure value is adjusted from 60 to 100 MPa to enable a fully contact of the tube, since the weld seam introduces a strengthened zone. Another modification is implemented in the 2 layers model loading path. The fourth step of axial feeding is modified from 10 mm to 10.7 mm due to convergence problems. A predominance of just one wrinkle formed from the axial feeding punch side is verified for 2 and 3 layers model. For 1 layer model, 2 wrinkles were formed but the wrinkle of the right side becomes more detached in the next steps.

As it was expected, the weld bead showed a higher stress values, since representing a location with strengthened material. In Table 5.6, it is visually difficult to spot those localized stresses. So, a zoom of the weld zone stresses is given in the figure 5.14. The localized stresses on the 1 layer model are higher than the remaining models, which seem to be in agreement with each other. Taking into account a more general evaluation of the stresses, the same conclusions are observed for the bulge zone.

As for the plastic strain, the set models seemed to share identical levels. Yet, near the weld location, there is a specific zone which proved to be more susceptible to necking when the weld bead inclusion is considered. By checking figure 5.14, it is visible the similarities of the patterns of each model. Once again, the 2 and 3 layers model indicated more conformity between them. In Kim *et al.* [40], similar patterns indicating the distribution of a ductile fracture value are found for a bulge model with weld bead and HAZ defined. However, two aspects must be considered: the axial feeding strategy and material properties disposition. Kim *et al.* conducted an experiment with both punches moving simultaneously, whereas only one side is used in the present bulge models. On the other hand, the weld bead and, particularly, the HAZ was wider when compared to the material regions defined in the current section.

Since the axissymetric condition is no longer valid, two sections are focused to evaluate the thickness variation. Specifically, the longitudinal section along the weld zone and the opposite section which corresponds to a base material zone, both sharing the same plane of symmetry. The two sections are identified as top and bottom section based on the tube's position displayed in the tables. In contrast with the previous thickness measurements, the models of this set show a thickening along the weld bead. This can be caused by the increased material hardness in the weld zone. On the opposite side, the bottom section shows final thickness values similar to the previous set with the same low carbon steel. Since 2 and 3 layers models revealed the same forming progression, their thickness curves are in agreement with each other in both top and bottom graphics. The 1 layer model case has a slightly different forming compared with the others, which justify the distinct thickness variations in top and bottom thickness graphics.

At figure 5.15, the processing times of the simulations are indicated. The increase of the central processing unit (CPU) time was expected when the weld seam is included. As it is observed, the time boost appears to be significant, rising by increasing the number of elements, i.e. the number of degrees of freedom in the numerical analysis. However, this increase is not exponential when considered the ratio between seamed and seamless homologous sets for instance, seamed tube 1 layer set/ seamless tube 1 layer set.

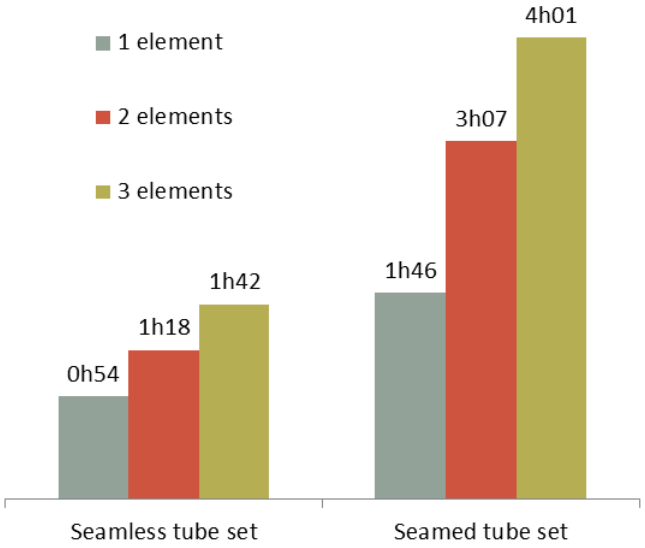

(a)

Ratio of the seamed/seamless set models	
1 element	2
2 elements	2,40
3 elements	2,36

(b)

Figure 5.15: CPU time of the simulations for S235JR bulged tubes: (a) absolute value (b) ratio between homologous models

5.4.4 Bulge conclusions

Based on the model's set discussion given, the most relevant conclusions can be summarized as:

- The effect of mesh refinement in thickness direction on the forming evolution prove to be inconclusive. For some sets, the 1 and 3 layers models are more coherent between them and, in other cases, the same is valid for 2 and 3 layers models. Although, higher stress levels were obtained for less refined meshes, which can indicate some level of volumetric locking effects;
- The inclusion of weld seam leads to a more realistic simulation, as it is confirmed by Kim *et al.* despite greater processing times. In the current simulations, the area near the HAZ is the most vulnerable to burst due the onset of necking.

Chapter 6

T-branched benchmark

Summary A more complex model (T-branched tube) is presented, being divided in two main parts. In a first one, a sensitivity study based on the type of elements of the die vs. the number of elements along the axial direction of the tube is carried out. In a second part, welded tube models are approached too. Strain and stress behaviour, thickness variation and instability appearance are the features aimed to be discussed and evaluated at the end of the chapter.

6.1 Model description

The model introduced in this chapter is a T-shaped component, designated for example by Manabe et al. [45]. This type of component is obtained by means of the displacement of two side punches aligned by the initial tube axis, and an internal fluid pressure. The transversal protrusion or shoulder to be filled has one counter-punch to facilitate the plastic forming of the material in the die and avoid unnecessary instabilities when it is movement is properly configured.

The model is divided in the same structure as the axissymetric model mentioned: die, tube and fluid. More precisely, the same simulation methodology used in the previous model was selected. The dimensions of the different components can be visualized in figure 6.1.

One major difference in the simulation step process compared to the previous chapter is related with the pressure definition. Instead of solely applying pressure in one step and solely applying axial feeding in the next one, until the end of the simulation, this will be made simultaneously in the present case. Such method was chosen due to the loading paths shown in [45].

The effect of friction was neglected due to simplification purposes, and the material is defined as isotropic. The numerical simulation model is divided in two halves, representing both extremities. The most reduced model possible would be the one quarter example which it was not adopted. Additionally, the actual configuration enables the alternative used of axial punches, fact that was considered to be executed in early stages of this work.

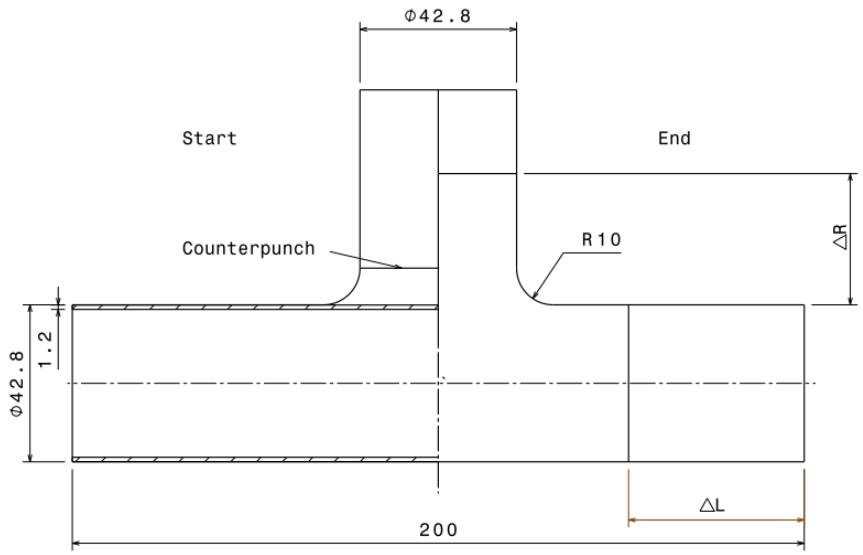

Figure 6.1: T-branched die and tube dimensions before (left) and after (right) hydroforming simulation process based on Manabe *et al* model [45] (measured in mm).

6.2 Sensitivity analysis

The sensitivity analysis presented in this section is not focused on the process parameters variation. Since it was not possible to conduct any experimental study, a sensitivity analysis of the parameters related with the numerical simulation seemed to be a suitable option. Among those, the focused parameters are the die's mesh and the tube's mesh. The die mesh configurations are divided into a purely triangular mesh (R3D3) and a mixed mesh between quadrangular (R3D4) and triangular elements - with a major number of quadrangular elements, as can be visualized in figure 6.4. As for the tube, there are two types of mesh refinement along the axial direction: with 3000 and 6000 elements.

Table 6.1: Properties of Aluminium Alloy 6063-T1 by Manabe *et al* [45].

Mechanical properties given	
Young's Modulus (GPa)	70
Yield stress (MPa)	50
n-value	0.32
Deduced by Ludwig-Hollomon equation: $\sigma = k\varepsilon^n$	
k	365.29 (MPa)

In order to carry out the simulations on this section, the material from the original model was applied (aluminium alloy A6063-T1) [45], as indicated in the table 6.1. Since Abaqus requires the plastic strain and the associated stress, the value of strength coefficient k was deduced based on Ludwig- Hollomon hardening law, also indicated in the table, and the true stress vs. true strain curve resulting from the hardening expression, shown in figure 6.2.

The applied loading path was an approximation of the non-linear loading path, which

is quite similar when matched with the respective curve in the original article. As visible in figure 6.3, the maximum axial feeding (ΔL) and counter-punch displacement (ΔR) are given as 48 mm and 25.7 mm, respectively, for a final pressure of 25 MPa.

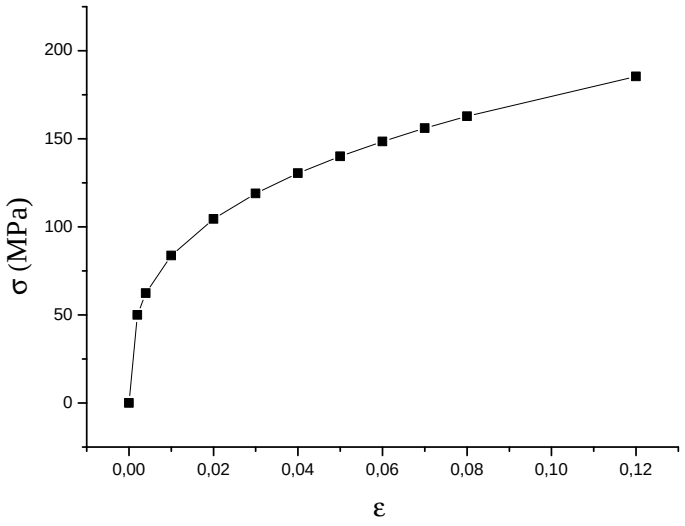

Figure 6.2: True stress vs. true strain curve of A6063-T1, based on the material properties given in Manabe *et al* [45].

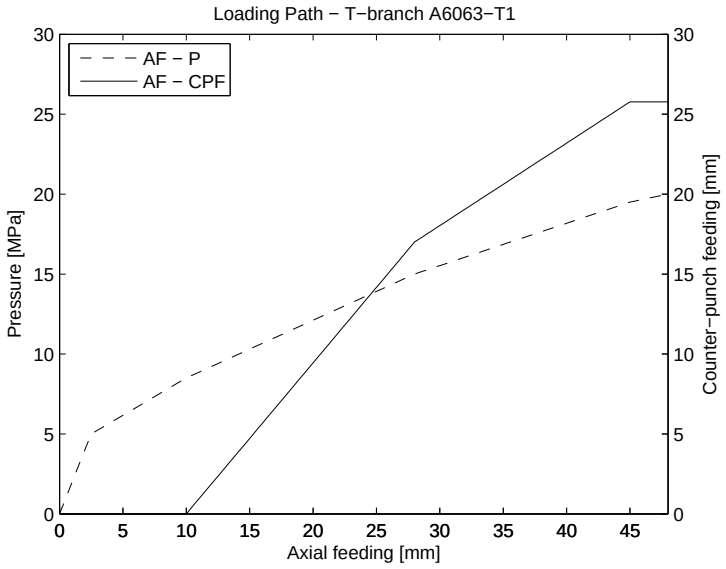

Figure 6.3: Loading path approximated from the one applied by Manabe *et al* [45].

An easier labelling of the models was performed at table 6.2 for an easier description throughout the chapter. The stress and strain color mapped images from the models executed in this subsection are shown in tables 6.3 and 6.4. Only C and D models were

represented, since both A and B models were very similar to the C model, and, for that reason, not considered in the results presentation.

Table 6.2: Label of sensitivity models.

Sensitivity set models		Type of die mesh	
		Mixed	Triangular
Number of tube elements	3000	A	B
	6000	C	D

Next, the final tube thickness on the two symmetric plane intersections were measured. The top location is the intersection on the die shoulder side (figure 6.6) while the bottom section is located at the opposite side (figure 6.7).

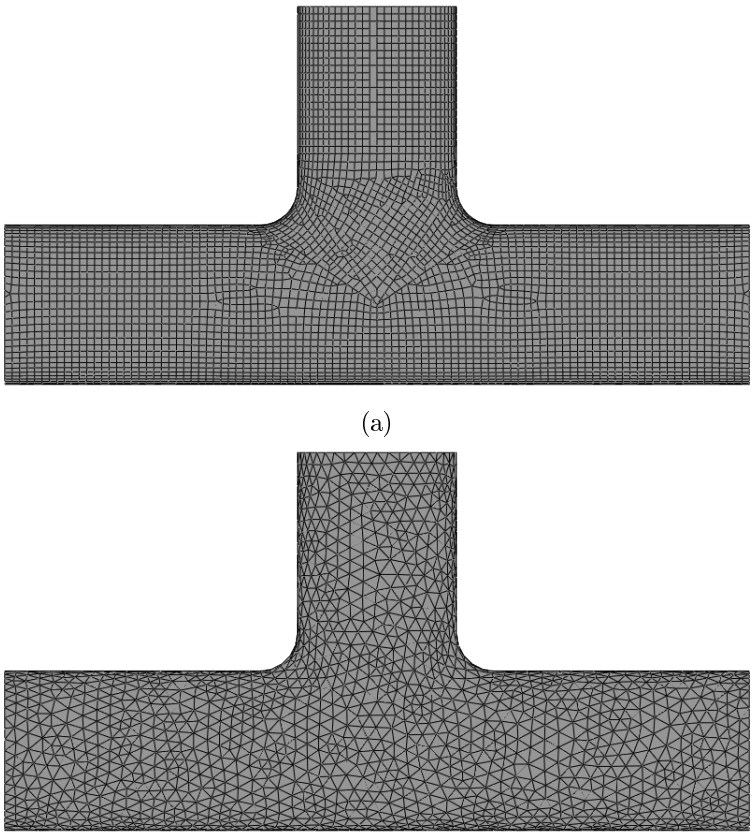

(a)

(b)

Figure 6.4: Type of mesh used for die discretization: a) Mixed die mesh b) Triangular die mesh.

Table 6.3: Von Mises stress between mixed mesh die and triangular die for 6000 tube element - Inside view

Step	C	D
1	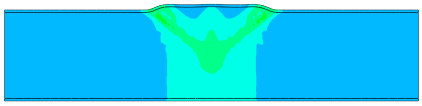	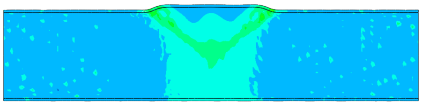
2	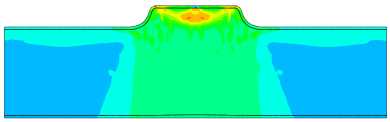	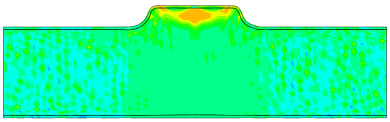
3	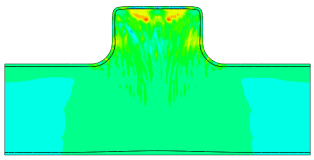	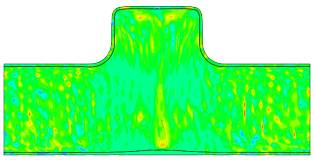
4	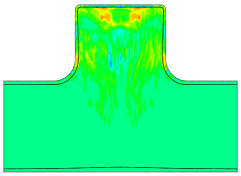	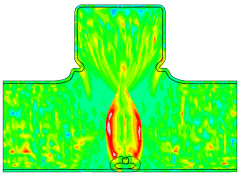
5	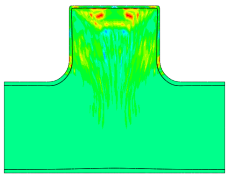	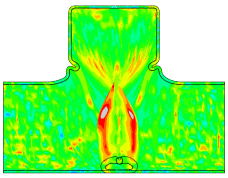

Table 6.4: Equivalent Plastic Strain (PEEQ) between mixed mesh die and triangular die for 6000 tube element - Inside view

Step	C	D
1		
2		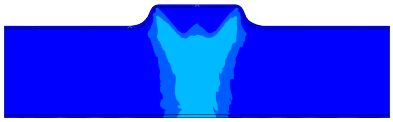
3	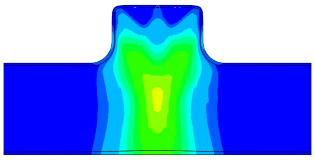	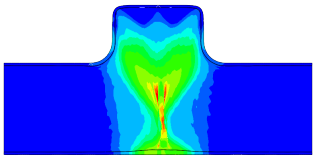
4	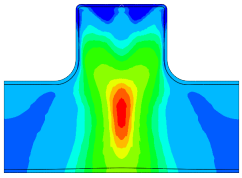	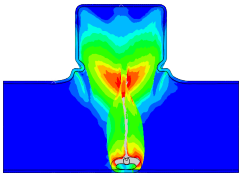
5	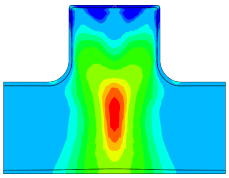	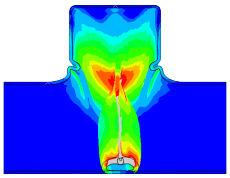

(a) Von Mises (b) PEEQ

Figure 6.5: Legend of the models in table 6.3 and 6.4

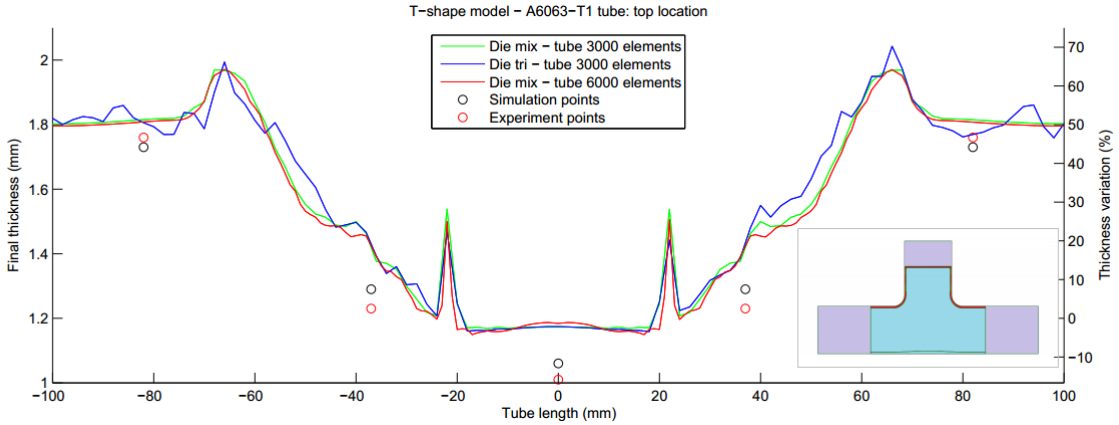

Figure 6.6: Absolute and percentage thickness values for the top location along the tube's length

.

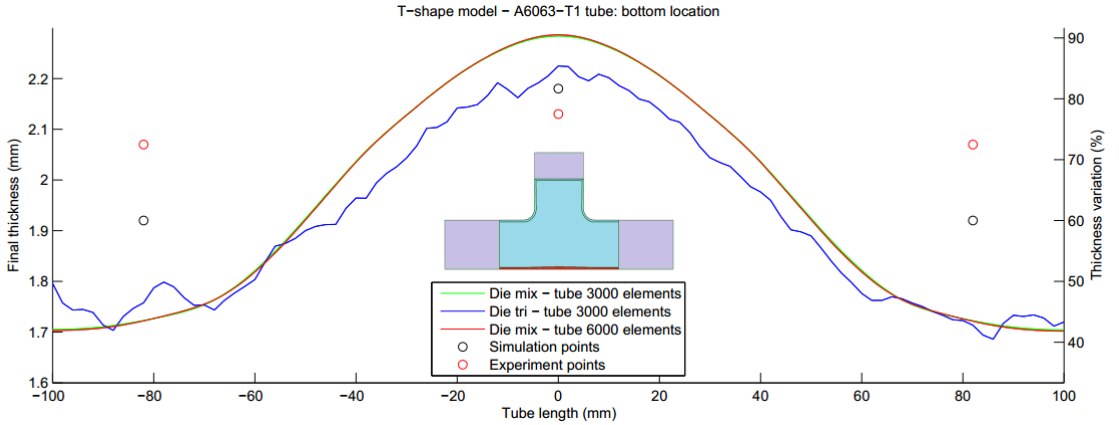

Figure 6.7: Absolute and percentage thickness values for the bot location along the tube's length

.

6.3 Seamless and seamed tubes

Similarly to the previous chapter, a study of the weld bead presence and location was also taken into account. To the expenses of losing the tube symmetry condition, it was only possible to simulate two tube positions: the position where tube's weld bead is turned to the die shoulder side (aligned with the symmetry plane, which is identified as top location) and the position where tube suffer an 180°rotation (identified as bottom location, both in figure 6.8. In other words, intermediate weld bead positions were not included into the numerical analysis. Once again, the low carbon steel S235JR is the material chosen whereas the weld bead properties are already known.

Regarding the results of the previous model, mixed die mesh and 200 elements in axial direction were defined for this model set. Additionally, instead of 1, 2 elements in radial direction were included, which dictates a total of 13200 and 12000 elements defining the tube, with and without weld seam, respectively. The same assumptions regarding the weld bead dimensions were also contemplated.

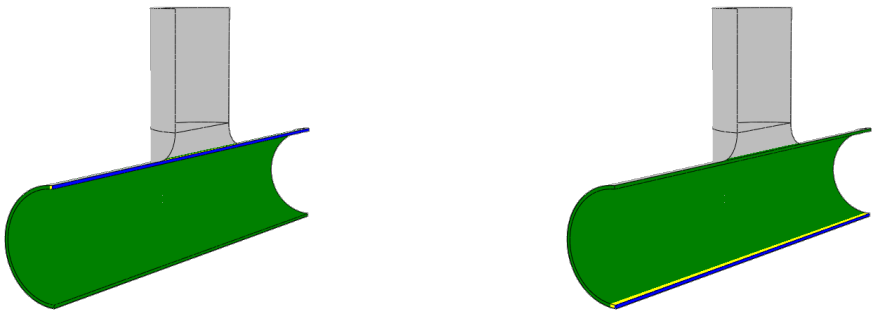

(a) (b)

Figure 6.8: Weld location for the T-shaped tube: (a) top (b) bottom.

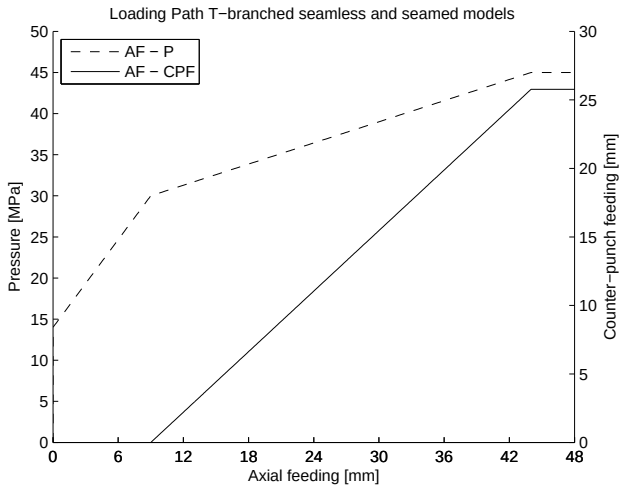

Figure 6.9: Loading path used for T-shaped seamless and seamed models of the current section.

A new loading path was implemented by trial and error process as it is demonstrated in figure 6.9 in order to obtain the requested tube final dimensions. Firstly, a small pressure is introduced, followed by a step with axial feeding and an increase of the internal pressure, enabling the material to flow to the counter-punch wall. At the third step, the counter-punch is also moved to the final position. The final adjustments in axial feeding and internal pressure are made in the last step.

In tables 6.5 and 6.6, the forming progression along the steps of the different models can be visualized with respective stress and strain color mapped images. The corresponding legend is located afterwards in figure 6.11. To compare the influence over the thickness variation, three graphs are exhibited: top and bottom thickness along the tube located at the symmetry plane, in figure 6.12 and 6.13, respectively, and the transversal thickness located at half of the tube's length in figure 6.14.

Table 6.5: Von Mises stress of the seamless tube model, top and bottom welded tube models - Inside view

Step	No weld	Bottom weld	Top weld
1			
2			
3	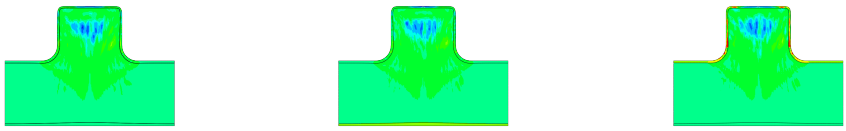		
4	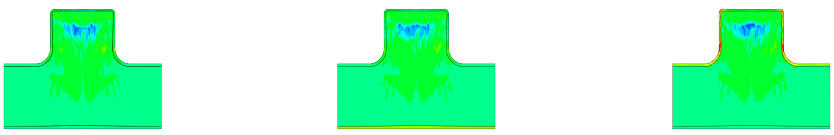		
4 - Iso	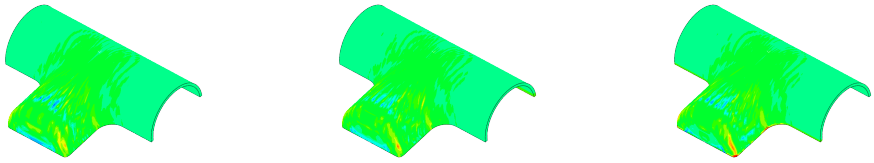		

Table 6.6: Equivalent Plastic Strain (PEEQ) of the seamless tube model, top and bottom welded tube models - Inside view

Step	No weld	Bottom weld	Top weld
1			
2			
3	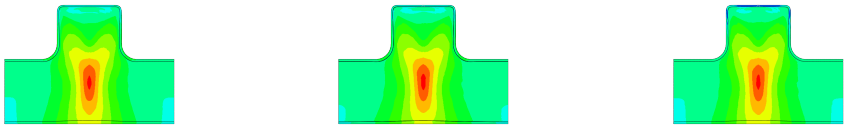		
4	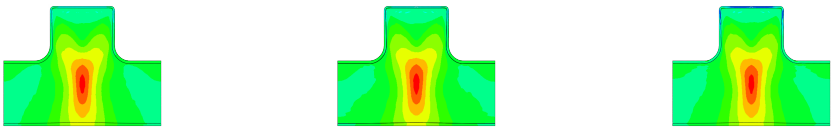		
4 - Iso	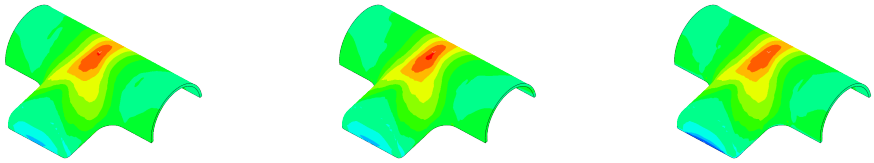		

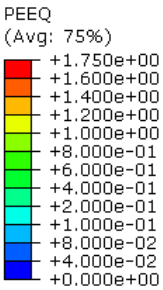

(a) PEEQ

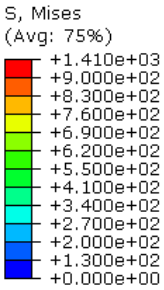

(b) Von Mises

Figure 6.10: Legend of the models in table 6.6 and 6.5

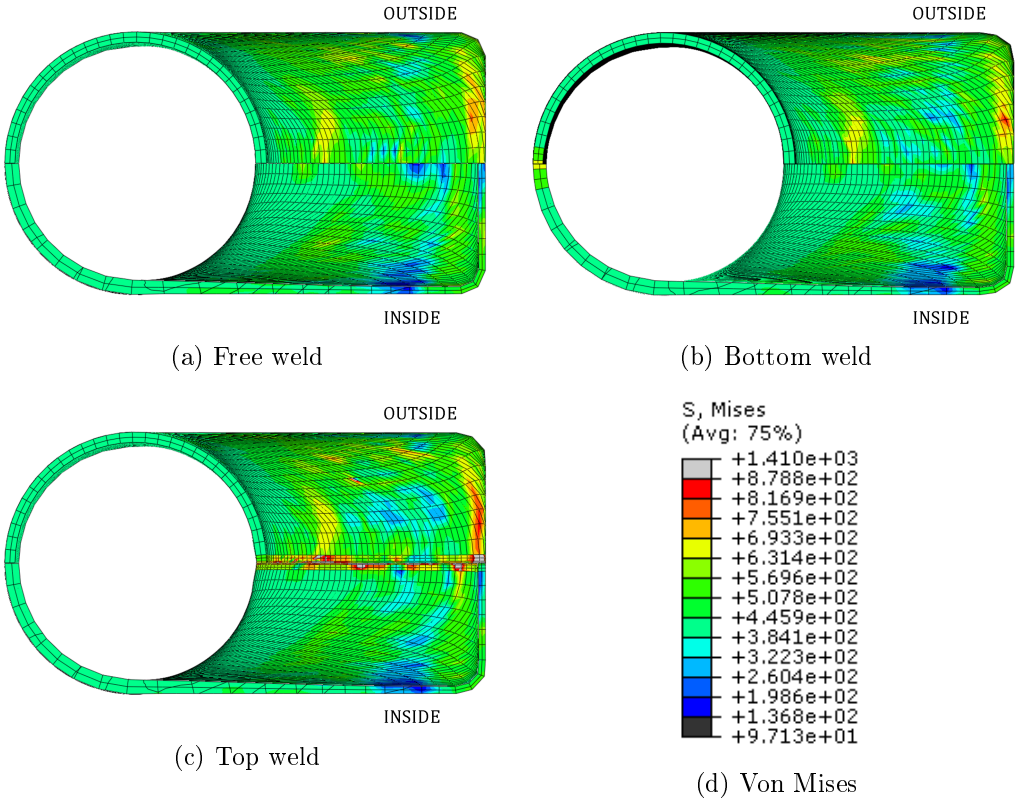

(a) Free weld

(b) Bottom weld

(c) Top weld

(d) Von Mises

Figure 6.11: Outside and inside view of 1/4 of T-branched final tubes to highlight the localized stresses.

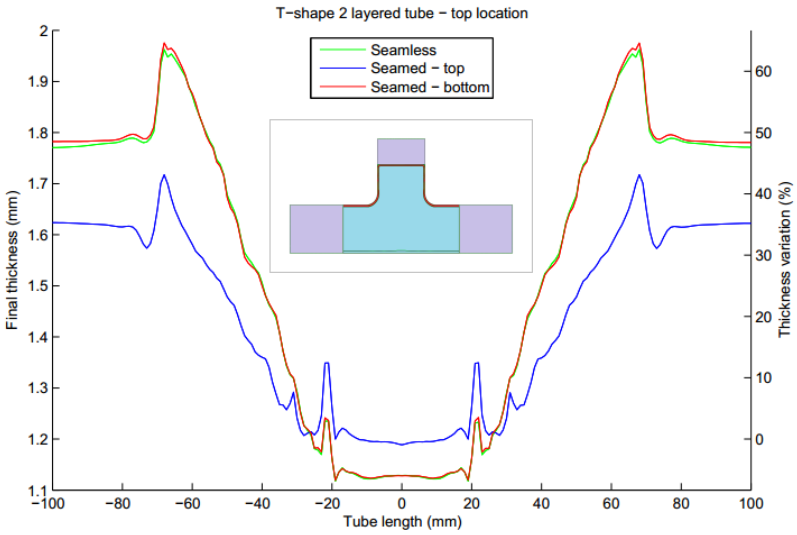

Figure 6.12: Final thickness and its variation for the S235JR T-branched models - Top location

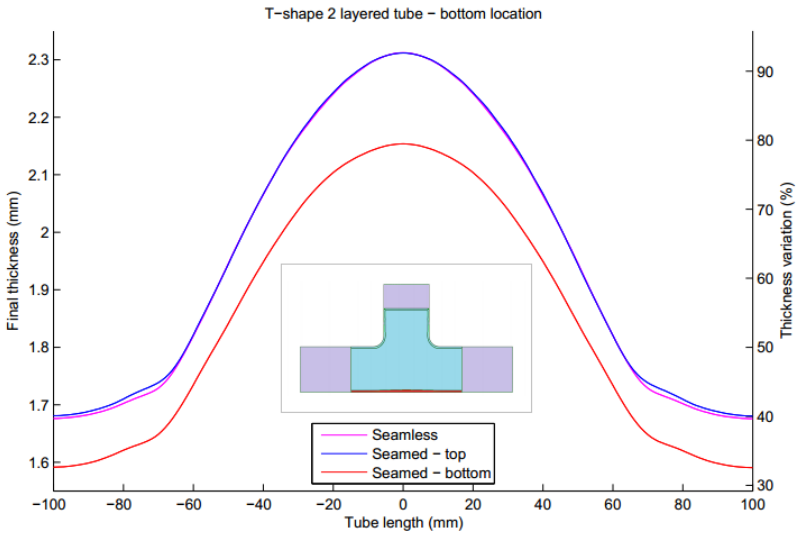

Figure 6.13: Final thickness and its variation for the S235JR T-branched models - Bottom location

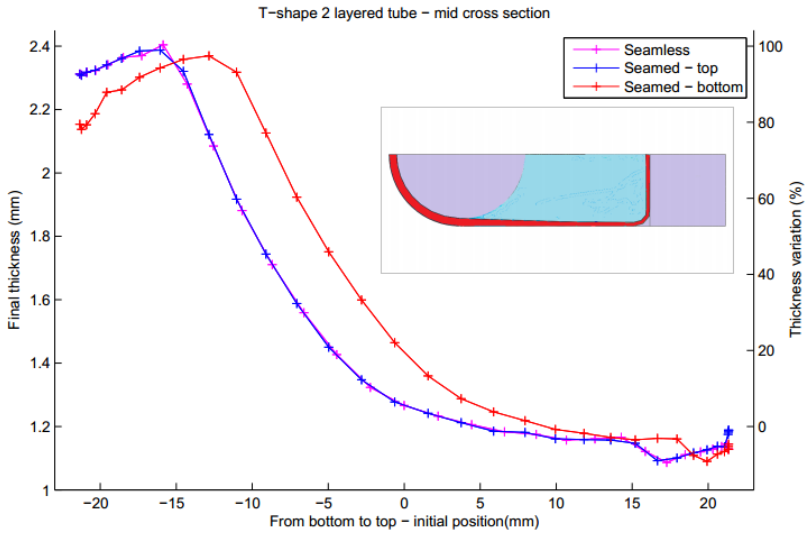

Figure 6.14: Final thickness and its variation for the S235JR T-branched models - Middle and transversal location

6.4 Analysis of results

6.4.1 Sensitivity analysis

From the sequence of images on tables 6.3 and 6.4, it is evident that the model D does not show a proper forming evolution during the numerical simulation. Apart from the remaining models, only this one developed an isolated wrinkle, which failed to be avoided with the loading path defined. The final result cannot be considered physically

acceptable. On the other hand, considering the proper forming, the tube's locations which experience higher stresses are the counter-punch contact zone and the die shoulder radius. The most critical location of the plastic deformation is found on the intersection of the tube axis and the axis of the die shoulder, easily spotted on images of table 6.4.

Focusing on the thickness behaviour in the models, a smoother representation of the thickness variation is shown for models where the die is defined by a majority of quadrilateral elements. This observation is verified in both graphics (figures 6.6 and 6.7). The model with a failed forming configuration was excluded from this study. Manabe's experimental and simulation values are also indicated. Manabe's simulation points reveal to be in agreement with its experimental points, only showing a small discrepancy among them. On the other hand, this discrepancy is augmented for the thickness curves obtained.

Focusing on the bottom thickness section, the experimental tube thickness was increased around 73% and stayed almost uniform along the tube. Albeit, the simulations points show a thicker value in central position and thinner values at locations near the tube sides. Following the Manabe's simulation tendency, an accentuated slope is verified for the simulation model curves from the extremities to the central location. For the top thickness section, a slight thickening is verified when compared Manabe's simulation with its experimental results. In models A, B and C, a more marked thickening is demonstrated. In other words, the conducted simulations do not describe the final thickness values accurately. With this in mind, it is important to mention that Manabe used a material with anisotropic properties, while, in the current work, the material was described with an isotropic yield criterion. Plus, the true stress vs. true strain curves deduced may also contribute for the different results.

Peaks of thickening are observed in the corner radius of the tube, more specifically at -65, -20, 20 and 65 mm in figure 6.6. Yet, the tube's corner radius near the counter-punch seemed to be most accentuated. According to the thickness distribution graphics presented, the addition of axial elements has no influence on thickness variation. Nevertheless, by looking at figure 6.15, the corner radius dimension at the counter-punch is reduced.

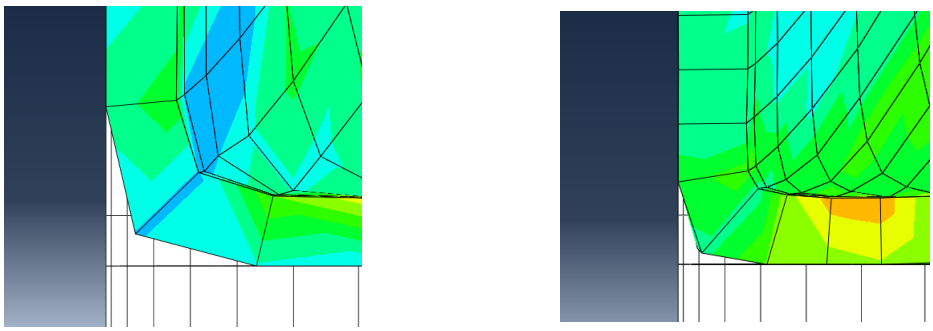

(a) 3000 elements (b) 6000 elements

Figure 6.15: Corner radius near counter-punch of the simulations performed.

Identically to the previous chapter, the CPU time is considered in the analysis as shown in figure 6.16. Apart from the better results obtained for the mixed mesh of the die, its processing times are also shorter for both simulation sets. Bearing this in mind, the

mixed mesh proves to be therefore a preferential option.

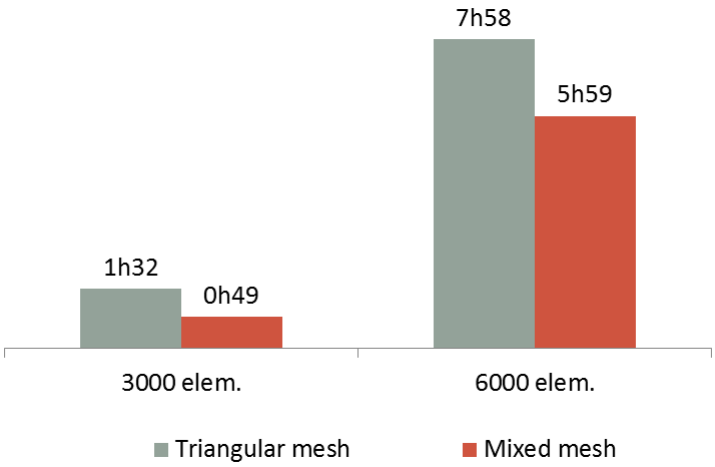

Figure 6.16: CPU time of the simulations for AA6063-T1 t-shaped tubes

6.4.2 Seamless and seamed tubes

For the second part of the current chapter, a different loading path was required and obtained by a trial-error method. In order to guarantee that the tube was already in contact with the die's wall before the axial feeding application, an initial pressure step of 15 MPa was defined. Consequently, both pressure and lateral punches displacement were applied until the tube's surface established a major contact with the immobilized counter-punch. Then, all parameters were set, so that the counter-punch was moved to its final position, without any instability problems. Finally, it was given a last axial feeding to achieve the desired tube's length.

Accordingly to the stress and strain tables (table 6.5 and 6.6), there is no significant variations between hydroformed components presented, at the first glance. Nevertheless, a few differences are detected. As seen before, the weld bead and HAZ represents a strengthened zone which induces localized stresses. For a more comprehensive reasoning, a different stress coloured map is applied to different views of the final component in figure 6.11. In figure 6.11a, which represents a seamless tube forming, the localized stresses are located around the corner radius area near the counter-punch at the plane of symmetry (orange zone) and a few centimetres down near the branch radius extremity (yellow zone). Identical coloured patterns are found for the final component with the weld seam, located in the inferior part of the T-branched die (figure 6.11b). Lastly, in figure 6.11c with the weld seam located at the superior part, the previous localized stresses are more pronounced, specially at the weld bead and HAZ location, reaching up values of 1410 MPa. In reality, the tube's bursting probably have occurred in previous stages due the high stress values displayed for the current loading path. However, without any failure criteria, it is impossible to infer about when the failure happened.

In terms of thickness variations, some obvious results were noted too. The following observations have the free weld model results as a reference point. Considering the longitudinal direction, for the model with the weld bead at the top location, thinner values on higher thickening rate locations and thicker values for higher thinning rate locations

were found, in opposition to the other models thickness behaviour at the same location (figure 6.12). As equivalent, the same observation was confirmed for the bottom location for the bottom weld model (figure 6.13). The models with no weld seam defined in the location to be analysed suffered a more evident thickening. As expected, this is caused by the different material properties (stiffness) associated to the weld bead. For both thickness measurement locations mentioned before, the thickness curves of the sections where the weld bead is not defined are in agreement with the no-weld model thickness curves. Additionally, as it is shown in figure 6.14, transversal thickness measurements infer that a welded tube, when placed with its weld turned down (180°), results on a different thickness distribution in comparison to the remaining models. Generally, the values of final thickness are higher in bottom location and decrease towards the counter-punch direction (top location). Firstly, the top seamed model shows practically no changes from the seamless tube simulation results. However, an increased thickening is observed in the formed branch wall thickness at the bottom seamed model, whereas its effect is more pronounced around -15 mm to 18 mm of the tube's transversal section. On the other hand, the seamless and top seamed models present a higher thickening at the bottom zone. Globally, the T-shaped components suffer a well-marked thickening and a very small thinning at the protrusion ends compared to the initial tube thickness (1.2 mm).

Finally, the CPU time of the executed models in the current subsection is displayed in figure 6.17. Naturally, an increase of the processing time is detected once a weld seam is defined. Plus, the model with the weld seam at the top location presents higher processing time than the model with the weld seam located at the bottom of the the die, once the stress states are completely different at the two zones.

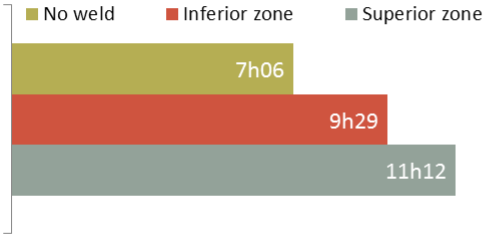

(a)

Ratio of the seamed/seamless set models	
Inferior zone	1,34
Superior zone	1,58

(b)

Figure 6.17: CPU time of the simulations for S235JR t-shaped tubes: (a) absolute values (b) ratio from seamed/seamless models

6.4.3 T-branched conclusions

From the results observed and discussed in this chapter, the following general conclusions for this example can be pointed out:

- Numerical simulations for this configuration seems to be sensitive to the type of mesh applied in the die. A fully triangular rigid elements (R3D3) mesh manifests lower and less smoother thickness variation for all the measured locations com-

pared with the mesh defined with a majority of R3D4 elements (and some R3D3 elements);

- Additional elements in axial direction defined a closer corner radius at counter-punch location but do not display any influence in thickness measurements, strain and stress levels obtained;
- The positioning of a longitudinally welded tube may be an aspect to considered, since lower stress levels are presented in the model with the weld seam at inferior location of the T-branched die. Plus, the bottom weld model thickness distribution present a major thickening effect at the center of the branch in circumferential direction.

Chapter 7

Final considerations

Summary In this last chapter, overall conclusions of the current work are succinctly presented. Hereupon, it is also enumerated some improvements to extend the developed research into future developments works.

7.1 Conclusions

This study aimed for an evaluation of the numerical simulation of hydroforming process of tubular components. In this regard, two benchmarks for THF were presented. The numerical work was carried out using Abaqus software, which is based on FEM. To describe the behaviour of the metallic materials adopted, isotropic plasticity criteria (von Mises) was considered. Multi-stage loading paths were applied to two benchmarks typically dealt with in literature. For the bulge benchmark, the pressure and axial feeding were separately applied, whereas it was simultaneous for the T- shaped benchmark. Distinct sensitivity analysis based on numerical parameters were conducted in both benchmarks, as well as an evaluation of the influence of a longitudinal weld seam, derived from tube manufacturing. Taking into account the results discussed during this document, the following conclusions can be presented:

- In both benchmarks, the inclusion of the longitudinal weld seam affected the strain and stress distribution, as well the thickness variation. For the bulge benchmark, the necking effects seemed to be more accentuated in the bulge zone near the HAZ, in contrast to the results of the seamless model sets;
- The positioning of the longitudinally welded tube seemed to affect the distribution of thickness for the T-branched benchmark, with major thickening of the T-shaped component in all the models. However, this feature is more pronounced in the model with the weld seam located at the bottom of the die, based on the loading path taken;
- In the bulge benchmark, the effect of mesh refinement in thickness direction is not clear due the divergences of wrinkles patterns among the models. Nevertheless, low mesh refinement seemed to induce higher stress levels;

- The sensitivity analysis conducted for the T-branched benchmark indicated smoother results of thickness values for the die whose mesh was defined predominately with R3D4 and a few R3D3 elements (mixed mesh), instead of the die with fully R3D3 elements (triangular mesh). By refining the tube's mesh, erroneous simulation results were obtained for the model with the triangular mesh type, while mixed mesh type refined model did not demonstrated any influence in thickness, stress and strain distributions.

7.2 Future developments

As future developments of the current work, some suggestions can be presented, such as:

- the development of a global three-dimensional thickness measurement strategy to completely represent the thickness distribution;
- the introduction of proper friction laws between tools and workpiece, which deeply influence the distribution of thickness and forming evolution;
- the consideration of distinct plasticity criteria and hardening models;
- the implementation of damage models and failure criteria, in order to predict defects such as bursting, as well increasing the feasibility of the numerical results;
- the application of optimization strategies to automatically calculate the ideal loading path;
- the study of more complex welded tube structures with pre-forming requirements, such as bending.

References

[1] F. Dohmann and Ch. Hartl. Hydroforming - a method to manufacture light-weight parts. *Materials Processing Technology*, vol.60:669–676, 1996.

[2] S. H. Zhang. Developments in hydroforming. *Journal of Materials Processing Technology*, vol.91:236–244, 1999.

[3] N. Asnafi and A. Skogsgardh. Theoretical and experimental analysis of stroke-controlled tube hydroforming. *Materials Science and Engineering*, A279:95–110, 2000.

[4] A. Alaswad, K.Y. Benyounis, and A.G. Olabi. Tube hydroforming process: A reference guide. *Materials & Design*, vol. 33:328–339, 2012.

[5] M. Koç. *Hydroforming for advanced manufacturing.* Woodhead Publishing Limited, Cambridge , England, 2009.

[6] Schuller GmbH. Metal Forming Handbook. pages 405–415. Springer Berlin Heidelberg, Berlin, 1998.

[7] M. Tolazzi. Hydroforming applications in automotive: a review. *International Journal of Material Forming*, vol. 3:307–310, 2010.

[8] M. Koç and T. Altan. An overall review of the tube hydroforming (THF) technology. *Journal of Materials Processing Technology*, vol. 108:384–393, 2001.

[9] A. Kocanda and H. Sadlowska. Automotive component development by means of hydroforming. *Archives of Civil And Mechanical Engineering*, Vol.3(3), 2008.

[10] SAE International. Hydroformed pillars are world first in 2013 Ford Fusion. `http://articles.sae.org/11393/`, Acessed January 2014.

[11] Complex. A,B and C pillars. `http://www.complex.com/sports/2013/03/25-car-terms-you-need-to-know/a-b-and-c-pillars`, Acessed November 2014.

[12] M. Ahmetoglu and T. Altan. Tube hydroforming : state-of-the-art and future trends. *Journal of Materials Processing Technology*, vol. 98:25–33, 2000.

[13] L. Lang, H. Li, S. Yuan, J. Danckert, and K.B. Nielsen. Investigation into the preforming's effect during multi-stages of tube hydroforming of aluminum alloy tube by using useful wrinkles. *Journal of Materials Processing Technology*, vol. 209(5):2553–2563, 2009.

[14] A. Ghosh, K. Deshmukh, and G. Ngaile. Database for real-time loading path prediction for tube hydroforming using multidimensional cubic spline interpolation. *Journal of Materials Processing Technology*, vol. 211(1):150–166, 2011.

[15] L. Lang, S. Yuan, X. Wang, Z.R. Wang, Z. Fu, J. Danckert, and K.B. Nielsen. A study on numerical simulation of hydroforming of aluminum alloy tube. *Journal of Materials Processing Technology*, vol. 146(3):377–388, 2004.

[16] A. S. Ponce. *Modelagem Experimental e controle do processo de hidroconformação de tubos.* Master thesis, Escola Politécnica da Universidade de São Paulo, 2006.

[17] F. J. Rípodas Agudo. Manufacturing Tubes For Hydroforming Applications. *Tube & Pipe Technology*, 2003.

[18] M. Merklein, M. Johannes, M. Lechner, and A. Kuppert. A review on tailored blanks - Production, applications and evaluation. *Journal of Materials Processing Technology*, vol. 214(2):151–164, 2014.

[19] G. N. Chu, G. Liu, S. J. Yuan, and W. J. Liu. Weld seam movement of tailor-welded tube during hydrobulging with dissimilar thickness. *The International Journal of Advanced Manufacturing Technology*, vol. 60(9-12):1255–1260, 2012.

[20] Tailor Welded Blank Project Team. Tailor welded blank applications and manufacturing - A state-of-the-art-survey. *The Auto/Steel Partnership*, 2001.

[21] R.M. Natal Jorge. *Modelação de Problemas Incompressíveis pelo Método das Deformações Acrescentadas baseado em Modos Compatíveis.* Phd thesis, Universidade do Porto, Porto, 1998.

[22] J. Rodrigues and P. Martins. *Tecnologia Mecânica - Tecnologia da Deformação Plástica, Vol. I Fundamentos teóricos.* Escola Editora, Lisboa, Portugal, 2nd edition, 2010.

[23] A. Mendelson. *Plasticity : Theory and Application.* R.E. Krieger Pub. Co, 1968.

[24] Yield surfaces in Haigh-Westergaard stress space. `http://en.wikipedia.org/wiki/Von_Mises_yield_criterion#mediaviewer/File:Yield_surfaces.svg`, Acessed June 2013.

[25] R.J. Alves Sousa. *Modelação de Problemas Incompressíveis pelo Método das Deformações Acrescentadas em Domínios Tridimensionais.* Master's thesis, Universidade do Porto, 2002.

[26] T. Jordão Grilo. *Estudo de modelos constitutivos anisotrópicos para chapas metálicas.* Master's thesis, Universidade de Aveiro, 2011.

[27] J.L. Alves. *Simulação numérica do processo de estampagem de chapas metálicas.* Phd thesis, Universidade do Minho, 2003.

[28] H.T. Carriço Mata. *Estudo de Estruturas Sandwich Hidroformadas Constituídas por Núcleo de Espumas Metálicas.* Phd thesis, Universidade do Porto, 2014.

[29] J. Chakrabarty. *Theory of Plasticity.* Elsevier Butterworth-Heinemann, 3rd edition, 2006.

[30] R. D. Cook, D. S. Malkus, M. E. Plesha, and R. J. Witt. *Concepts and Applications of Finite Element Analysis.* University of Wisconsin - Madison, 4th edition, 2002.

[31] K.J. Bathe. *Finite Element Procedures.* Prentice Hall, NewJersey, USA, 1996.

[32] F. Teixeira-Dias, J. Pinho-da Cruz, R.A Fontes Valente, and R.J. Alves de Sousa. *Método dos Elementos Finitos, Técnicas de Simulação Numérica em Engenharia.* ETEP, Lisboa, Portugal, 2010.

[33] R.W. Clough. The finite element method in plane stress analysis. In *Proceedings of the 2nd ASCE Conference on Electronic Computation*, pages 345–378, Pittsburg, USA, 1960.

[34] K.J. Bathe. Finite Element Method. In B. Wah, editor, *in Wiley Encyclopedia of Computer Science and Engineering*, pages 1253–1264. John Wiley & Sons, Inc., 2008.

[35] ABAQUS (2010). *ABAQUS 6.10 User's Manual.* Dassault Systèmes, Providence, RI, USA.

[36] L Gao, S Motsch, and M Strano. Classification and analysis of tube hydroforming processes with respect to adaptive FEM simulations. vol. 129:261–267, 2002.

[37] A. E. Tekkaya. State-of-the-art of simulation of sheet metal forming. *Journal of Materials Processing Technology*, vol. 103(1):14–22, 2000.

[38] ABAQUS (2010). *ABAQUS 6.10 - Interactive Edition.* Dassault Systèmes, Providence, RI, USA.

[39] D. Sornin, S. Fayolle, P.-O. Bouchard, and E. Massoni. Plastic instabilities analysis during T-shaped tubes hydro-forming process. *International Journal of Material Forming*, vol. 2(2):131–144, 2009.

[40] J. Kim, Y. Kim, B. Kang, and S. Hwang. Finite element analysis for bursting failure prediction in bulge forming of a seamed tube. *Finite Elements in Analysis and Design*, vol. 40:953–966, 2004.

[41] A. Khalfallah. Experimental and numerical assessment of mechanical properties of welded tubes for hydroforming. *Materials & Design*, 56:782–790, 2014.

[42] D. A. Oliveira and M. J. Worswick. Tube bending and hydroforming of aluminium alloy S-rails. *International Journal of Material Forming*, 2(3):197–215, 2009.

[43] M Ahmetoglu, K Sutter, X.J Li, and T Altan. Tube hydroforming: current research, applications and need for training. *Journal of Materials Processing Technology*, 98(2):224–231, 2000.

[44] A. P. Roque. *Study of the tubular hydroforming process.* Master's thesis, Universidade do Porto, 2005.

[45] K. Manabe, M. Suetake, H. Koyama, and M. Yang. Hydroforming process optimization of aluminum alloy tube using intelligent control technique. *International Journal of Machine Tools and Manufacture*, vol. 46(11):1207–1211, 2006.